



# Multiscale modeling of oriented thermoplastic elastomers with lamellar morphology

O. Lopez-Pamies<sup>a,b,1</sup>, R. Garcia<sup>c</sup>, E. Chabert<sup>b</sup>, J.-Y. Cavallé<sup>c</sup>, P. Ponte Castañeda<sup>a,\*</sup>

<sup>a</sup> Department of Mechanical Engineering and Applied Mechanics, University of Pennsylvania, Philadelphia, PA 19104-6315, USA

<sup>b</sup> LMS, UMR 7649, École Polytechnique, 91128 Palaiseau, France

<sup>c</sup> MATEIS, UMR 5510, INSA de Lyon, 69621 Villeurbanne, France

## ARTICLE INFO

### Article history:

Received 2 November 2007

Accepted 17 July 2008

### Keywords:

Block copolymers

Finite strain

Microstructures

Homogenization

Instabilities

## ABSTRACT

Thermoplastic elastomers (TPEs) are block copolymers made up of “hard” (glassy or crystalline) and “soft” (rubbery) blocks that self-organize into “domain” structures at a length scale of a few tens of nanometers. Under typical processing conditions, TPEs also develop a “polydomain” structure at the micron level that is similar to that of metal polycrystals. Therefore, from a continuum point of view, TPEs may be regarded as materials with heterogeneities at two different length scales. In this work, we propose a constitutive model for *highly oriented, near-single-crystal TPEs with lamellar domain morphology*. Based on small-angle X-ray scattering (SAXS) and transmission electron microscopy (TEM) observations, we consider such materials to have a granular microstructure where the grains are made up of the same, perfect, lamellar structure (single crystal) with slightly different lamination directions (crystal orientations). Having identified the underlying morphology, the overall finite-deformation response of these materials is determined by means of a two-scale homogenization procedure. Interestingly, the model predictions indicate that the evolution of microstructure—especially *the rotation of the layers*—has a very significant, but subtle effect on the overall properties of near-single-crystal TPEs. In particular, for certain loading conditions—namely, for those with sufficiently large compressive deformations applied in the direction of the lamellae within the individual grains—the model becomes macroscopically unstable (i.e., it loses strong ellipticity). By keeping track of the evolution of the underlying microstructure, we find that such instabilities can be related to the development of “chevron” patterns.

© 2008 Elsevier Ltd. All rights reserved.

## 1. Introduction

Thermoplastic elastomers (TPEs) are a special class of block copolymers that exhibit unique mechanical behavior ranging from that of thermoplastics to elastomers. Due to their superior tailoring and recycling properties with respect to conventional cross-linked rubbers, TPEs are increasingly being used in commercial applications (e.g., footwear, automotive, medical, etc.). In addition, because of their self-assembling properties, TPEs have also been proposed (see, e.g., Park et al., 2003; Bockstaller et al., 2005) as promising candidates in nanotechnological applications. The unique properties of these materials stem from their hierarchical structure (see, e.g., Honeker and Thomas, 1996). More precisely, TPEs are made up of

\* Corresponding author.

E-mail addresses: [oscar.lopez-pamies@sunysb.edu](mailto:oscar.lopez-pamies@sunysb.edu) (O. Lopez-Pamies), [ponte@seas.upenn.edu](mailto:ponte@seas.upenn.edu), [ponte@lms.polytechnique.fr](mailto:ponte@lms.polytechnique.fr) (P. Ponte Castañeda).

<sup>1</sup> Currently in the Department of Mechanical Engineering, State University of New York, Stony Brook, NY 11794-2300, USA.

“hard” (glassy or crystalline) and “soft” (rubbery) blocks that *self-assemble* at the *nanometer scale* into a wide range of morphologies (Fredrickson and Bates, 1996). Several studies have been published recently concerning the mechanical properties of TPEs where the hard blocks self-organize to form spherical particles (Prasman and Thomas, 1998), cylindrical fibers (Honeker et al., 2000), interconnected networks (Dair et al., 1999), and layers (Cohen et al., 2000). Furthermore, under typical processing conditions, TPEs also develop a “granular” structure at the *micron level* (Seguela and Prud’homme, 1981; Gido et al., 1993), which is similar to that of metal polycrystals. In view of their increasing commercial importance and substantial potential for utilization in emerging technologies, it is of practical interest to develop constitutive models for the mechanical behavior of these material systems. This is the main objective of this paper. In particular, in this work, we will be concerned with the constitutive modeling of *highly oriented, near-single-crystal (NSC) TPEs with lamellar morphology*.

One of the first studies of oriented TPEs with lamellar morphology is that of Allan et al. (1991), who examined both *experimentally* and *theoretically* the mechanical response of polystyrene–polybutadiene–polystyrene (SBS) triblock-copolymer films subjected to *small deformations*. In their modeling, these authors idealized SBS films as perfect laminates made up of alternating layers of two different linearly elastic, isotropic materials. By making use of well-known results from linear homogenization theory, they computed the overall elastic moduli of these materials. Their model predictions were shown to be in excellent agreement with the experimental results. In a later contribution, Read et al. (1999) (see also Polis and Winey, 1998) carried out a combined *analytical* and *numerical* study of the behavior of two-dimensional (2D) oriented TPEs subjected to tensile loading in the perpendicular direction to the lamellae. They focused on the possible buckling of the layers and its connection with the development of “chevron” patterns (or zig-zag structures). It should be mentioned that, unlike Allan et al. (1991), Read et al. (1999) did account for *finite deformations* in their modeling, but they did so in an approximate manner. More recently, Cohen et al. (2000) have provided a thorough *experimental* characterization of the behavior of NSC SBS films subjected to *finite deformations*. More specifically, these authors have provided macroscopic stress–strain measurements, together with *in situ* small-angle X-ray scattering (SAXS) and microscopy observations, for oriented SBS films subjected to uniaxial tension loadings at different orientations relative to the lamination direction. Finally, Tzianetopoulou and Boyce (2004) have conducted plane-strain *numerical simulations* for the mechanical response of oriented TPEs subjected to *large deformations normal and parallel to the lamellae*. Motivated by the experimental findings of Cohen et al. (2000), they considered oriented TPEs as laminates—made up of alternating layers of two different nonlinear materials—with a variety of morphological imperfections, such as lamellar waviness and interface/interphase imperfections.

In this work, we develop a *three-dimensional (3D) constitutive model* for oriented TPEs with lamellar morphology subjected to *general finite deformations*. More specifically, based on experimental evidence (see Section 2), we consider this class of materials to be granular systems whose grains are made up of the same, perfect, lamellar structure (single crystal, SC) with slightly different lamination directions (crystal orientations). In other words, we assume that the orientation distribution function (ODF) is highly textured. Furthermore, the hard and soft blocks that make up the lamellar structures within the grains are taken to be characterized by hyperelastic potentials, so that dissipative effects are neglected. (Note that in spite of adopting a non-dissipative framework, it is still possible to consider approximately plastic behavior within the context of deformation theory of plasticity.) Under the above geometric and constitutive hypotheses, the model for oriented TPEs is then constructed by means of a two-scale homogenization procedure. Thus, the effective behavior of the grains—which are assumed to be made up of perfect lamellar structures—will be determined from well-known results (see, e.g., Triantafyllidis and Maker, 1985; Triantafyllidis and Nestorvić, 2005). Then, the “tangent second-order” homogenization method (Ponte Castañeda, 1996; Ponte Castañeda and Willis, 1999; Ponte Castañeda and Tiberio, 2000) will be used to generate estimates for the overall behavior of the entire granular structure. In this regard, it should be emphasized that the tangent second-order homogenization technique has the capability to account for statistical information on the *initial* microstructure beyond the ODF, as well as for its *evolution*, which results from the finite changes in geometry that are induced by the applied finite deformations. This point is crucial as the evolution of the microstructure can have a significant geometric softening (or stiffening) effect on the overall response of the material, which, in turn, may lead to the possible development of macroscopic instabilities. In addition, this homogenization technique has the distinguishing feature of being *exact* to second order in the heterogeneity contrast (see also Ponte Castañeda and Suquet, 1998). This feature is particularly useful within the context of the present work, since oriented TPEs with lamellar morphology may be considered as granular materials with a *small “crystal” heterogeneity contrast* (see Section 2). Parenthetically, it should also be mentioned that a more accurate version of the “second-order” homogenization theory including field fluctuations (Ponte Castañeda, 2002; Lopez-Pamies and Ponte Castañeda, 2006a) has already been employed to generate constitutive models for various types of elastomeric composites, including reinforced elastomers (see, e.g., Lopez-Pamies and Ponte Castañeda, 2006a, b; Brun et al., 2007). These models have been shown to be in good agreement with corresponding exact and numerical results available from the literature for special loading conditions. In this connection, it should be clarified that the earlier tangent second-order method of Ponte Castañeda and Tiberio (2000)—as opposed to the more accurate second-order method of Lopez-Pamies and Ponte Castañeda (2006a)—is utilized here for computational simplicity, since both methods can be shown to lead to essentially the same results when specialized to the class of TPEs of interest in this work (basically because both methods are exact to second order in the heterogeneity contrast, which is precisely the case of interest here).

This paper is organized as follows. Section 2 describes in some detail the structure of typical oriented TPEs with lamellar morphology by means of transmission electron microscopy (TEM) and SAXS. Having identified the material system of

interest, Section 3 discusses certain theoretical considerations including the definition of effective properties and a brief summary of the tangent second-order homogenization method. Section 4 then provides the main result of this paper: a constitutive model for the overall behavior of *highly oriented*, NSC TPEs. The principal features of this model are discussed within the context of a model problem, as well as within preliminary comparisons with experimental measurements in Sections 5 and 6. In this regard, it should be mentioned that more detailed comparisons of the proposed model with experimental results will be presented elsewhere. The emphasis in this paper is on the identification and the modeling of the underlying physical mechanisms. Finally, some general conclusions are drawn in Section 8.

## 2. Typical structure of oriented TPEs with lamellar morphology

In this section, we characterize the structure of oriented SBS triblock copolymers with lamellar morphology—arguably the most commercially used class of lamellar TPEs—by means of TEM and SAXS. The raw material chosen for our study is a commercially available SBS triblock copolymer containing 42% volume fraction of polystyrene (PS). It should also be mentioned that the TEM images and SAXS measurements to be presented subsequently correspond to specimens (see Fig. 1) that were prepared via a roll-casting process (Albalak and Thomas, 1993). A complete description of the raw material, specimen preparation, TEM imaging, and SAXS measurements can be found in Garcia (2006). With the construction of a homogenization-based constitutive model as main objective, we focus here on outlining the principal structural features of oriented TPEs with lamellar morphology.

Fig. 2 shows a typical TEM image of the front section (i.e., the  $\mathbf{e}_1$ – $\mathbf{e}_2$  plane in Fig. 1) of an oriented SBS film, where the dark phase corresponds to the polybutadiene (PB). An immediate observation from this figure is the high degree of order and orientation of the layers. The sample is not free of defects, however. Note for instance the presence of two major regions (or grains) with slightly different lamination directions. Note further that the lamellae are not completely straight within the grains, but instead, they appear to have some waviness. The existence of other defects such as “edge dislocations” has also been suggested by other imaged regions. It should be emphasized that all of these observations are in agreement with the earlier findings of Cohen et al. (2000).

Fig. 3 shows SAXS measurements obtained by irradiation into the front section (i.e., into the  $\mathbf{e}_1$ – $\mathbf{e}_2$  plane in Fig. 1) of an oriented SBS film. Part (a) shows the 2D SAXS pattern. Part (b) illustrates the corresponding intensity  $I$  as a function of the azimuthal angle  $\varphi$ . Finally, part (c) shows the intensity profile as a function of the lamellar spacing (or repeat length of the layers)  $d$ . In connection with this last part, it should be mentioned that the geometrical variable  $d$  was computed directly from measured values of the scattering vector  $q$  by making use of Bragg’s law:  $q = 2\pi/d$ .

The main observation from the SAXS pattern shown in Fig. 3(a) is the existence of several Bragg reflections, which confirms the high degree of lamellar orientation already observed in the TEM. It is crucial to recognize, however, that there is *not* a unique lamination direction in the film, but instead, as illustrated in Fig. 3(b), there is a continuous distribution of slightly different lamination directions. Indeed, the intensity  $I$  in Fig. 3(b)—which can be identified essentially with the distribution function of lamination directions in the sample—is seen to have a “bell shape” of *finite width*. In this regard, it is important to remark that the maximum deviation from the average lamination direction in the film is seen to be approximately  $10^\circ$ .

Having described the lamellar orientation in (the front section of) the SBS film, we next describe the other piece of structural information that can be readily deduced from the SAXS measurements: the repeat length of the layers. To this end, we turn our attention to Fig. 3(c). Similar to Fig. 3(b), we observe that the intensity  $I$  in this figure—which in this case can be identified essentially with the distribution function of repeat length of the layers in the sample—also has a “bell shape” of finite width. In this connection, we observe from this plot that the average repeat length in the film is 26.7 nm and that the maximum deviation from this average is approximately 2 nm.

At this point, it is important to state that TEM images and SAXS measurements have also been obtained (see Garcia, 2006) for the side section of the SBS film (i.e., the  $\mathbf{e}_2$ – $\mathbf{e}_3$  plane in Fig. 1). The corresponding results are very similar to those presented here for the front side, but with a sizeably higher degree of lamellar orientation.

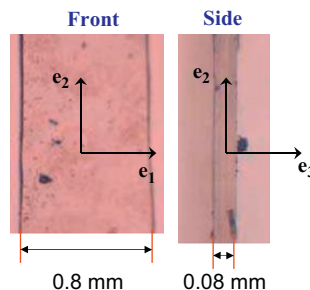
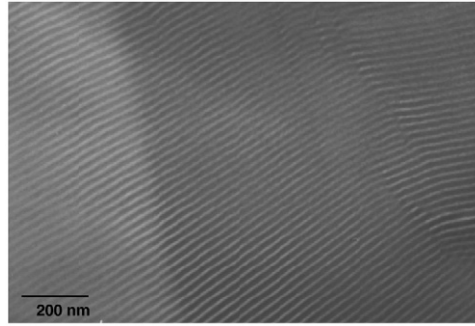
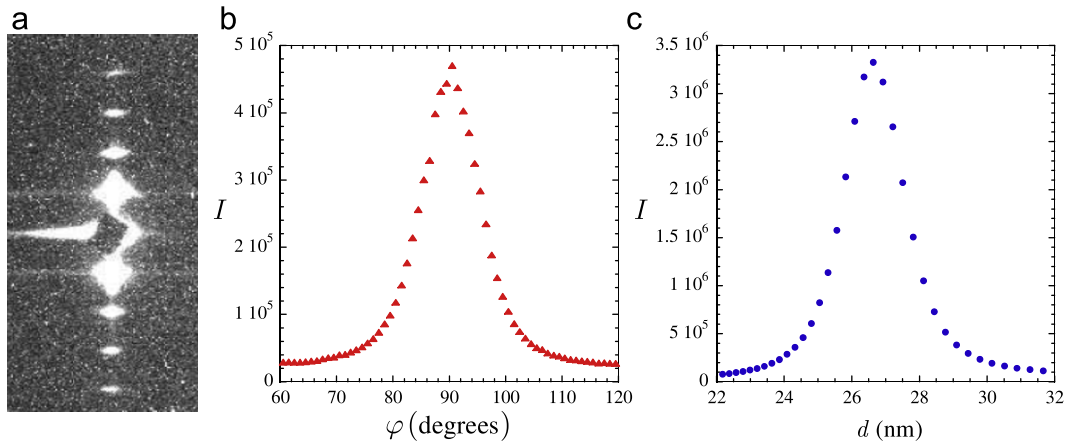


Fig. 1. Pictures of the front and side views of an oriented SBS triblock-copolymer film, with the corresponding dimensions. Note that the front view has been identified with the  $\mathbf{e}_1$ – $\mathbf{e}_2$  plane, while the side view corresponds to the  $\mathbf{e}_2$ – $\mathbf{e}_3$  plane.



**Fig. 2.** TEM image of the front section (i.e., the  $\mathbf{e}_1$ – $\mathbf{e}_2$  plane in Fig. 1) of an oriented SBS film. The sample was stained with osmium tetroxide ( $\text{OsO}_4$ ), rendering the PB phase dark in the image.



**Fig. 3.** SAXS measurements obtained by irradiation into the front section (i.e., into the  $\mathbf{e}_1$ – $\mathbf{e}_2$  plane in Fig. 1) of an oriented SBS film. (a) 2D SAXS pattern. (b) Intensity  $I$  as a function of the azimuthal angle  $\varphi$ . (c) Intensity  $I$  as a function of lamellar spacing (or repeat length of the layers)  $d$ .

In summary, the experimental results presented in this section suggest that the oriented TPEs with lamellar morphology of interest in this work are actually made up of a granular *microstructure* whose grains, in turn, are made up of a lamellar *nanostructure* of alternating layers of hard and soft blocks. The lamellae within the grains are not perfect in the sense that they exhibit a small amount of waviness, as well as other type of defects, such as edge dislocations. Moreover, the direction of lamination and lamellar spacing are not uniform throughout the material, but instead, they exhibit a continuous—yet narrow—distribution of values.

It is plain that all of the above-identified structural features may play a more or less significant role in the overall mechanical behavior of oriented TPEs with lamellar morphology. In this regard, we believe that perhaps the most dominant feature—which needs to be accounted for in order to generate accurate constitutive models for these materials—is the distribution of different lamination directions. Thus, in this work, we will idealize the morphology of oriented TPEs as granular structures whose grains are made up of the same, perfect, lamellar structure—or SCs—with slightly different laminations directions—or crystal orientations (see Section 4 for further details). The validity of this idealization—which neglects the effects of lamellar waviness within the grains, edge dislocations, and variations in the repeat length of the layers—will be addressed in this work by means of theoretical results and qualitative comparisons with experiments, as well as with more thorough comparisons with experimental measurements elsewhere.

### 3. Preliminaries on homogenization

Consider a solid made up of a statistically uniform distribution of two<sup>2</sup> different “homogeneous” phases. A specimen of this material is assumed to occupy a volume  $\Omega_0$ , with boundary  $\partial\Omega_0$ , in the undeformed configuration. Furthermore, the characteristic length of the underlying inhomogeneities (e.g., layers, grains) is assumed to be much smaller than the size of the specimen and the scale of variation of the applied loading.

<sup>2</sup> For the purpose of this work, as it will become more clear below, it suffices to restrict attention to two-phase composites.

Material points in the solid are identified by their initial position vector  $\mathbf{X}$  in the reference configuration  $\Omega_0$ , while the current position vector of the same point in the deformed configuration  $\Omega$  is given by  $\mathbf{x}$ . The deformation gradient  $\mathbf{F}$  at  $\mathbf{X}$ , a quantity that measures the deformation in the neighborhood of  $\mathbf{X}$ , is defined by

$$\mathbf{F} = \frac{\partial \mathbf{x}}{\partial \mathbf{X}}, \quad J = \det \mathbf{F} > 0 \text{ on } \Omega_0. \quad (1)$$

The constitutive behaviors of the phases, which occupy the subdomains  $\Omega_0^{(1)}$  and  $\Omega_0^{(2)} = \Omega_0 - \Omega_0^{(1)}$  in the undeformed configuration, are characterized by stored-energy functions  $W^{(1)}$  and  $W^{(2)}$  that are *objective, non-convex* functions of the deformation gradient tensor  $\mathbf{F}$ . Thus, the local stored-energy function of the composite may be conveniently written as follows:

$$W(\mathbf{X}, \mathbf{F}) = \sum_{r=1}^2 \chi_0^{(r)}(\mathbf{X}) W^{(r)}(\mathbf{F}), \quad (2)$$

where the characteristic functions  $\chi_0^{(r)}$ , equal to 1 if the position vector  $\mathbf{X}$  is inside phase  $r$  (i.e.,  $\mathbf{X} \in \Omega_0^{(r)}$ ) and zero otherwise, describe the distribution of the two phases in the reference configuration. Note that  $\chi_0^{(r)}$  may be *periodic* or *random*. In the first case, the dependence of  $\chi_0^{(r)}$  on the position vector  $\mathbf{X}$  is completely known. In the second case, the dependence of  $\chi_0^{(r)}$  on  $\mathbf{X}$  is not known precisely, and the microstructure is only partially defined in terms of the  $n$ -point statistics of the system. In this work, use will be made of information up to only two-point statistics in order to be able to take advantage of linear homogenization estimates that are available from the literature. The local or microscopic constitutive relation for the composite is given by

$$\mathbf{S} = \frac{\partial W}{\partial \mathbf{F}}(\mathbf{X}, \mathbf{F}), \quad (3)$$

where  $\mathbf{S}$  denotes the first Piola–Kirchhoff stress tensor, and sufficient smoothness has been assumed for  $W$  on  $\mathbf{F}$ .

Following Hill (1972), the global or macroscopic constitutive relation for the composite is then given by

$$\bar{\mathbf{S}} = \frac{\partial \bar{W}}{\partial \bar{\mathbf{F}}}, \quad (4)$$

where  $\bar{\mathbf{S}} = \langle \mathbf{S} \rangle$ ,  $\bar{\mathbf{F}} = \langle \mathbf{F} \rangle$  are the *average stress* and *average deformation gradient*, respectively, and

$$\bar{W}(\bar{\mathbf{F}}) = \min_{\mathbf{F} \in \mathcal{K}(\bar{\mathbf{F}})} \langle W(\mathbf{X}, \mathbf{F}) \rangle = \min_{\mathbf{F} \in \mathcal{K}(\bar{\mathbf{F}})} \sum_{r=1}^2 c_0^{(r)} \langle W^{(r)}(\mathbf{F}) \rangle^{(r)} \quad (5)$$

is the *effective stored-energy function* of the composite. In the above expressions, the brackets  $\langle \cdot \rangle$  and  $\langle \cdot \rangle^{(r)}$  denote volume averages (in the undeformed configuration) over the specimen,  $\Omega_0$ , and over the phase  $r$ ,  $\Omega_0^{(r)}$ , respectively, so that the scalars  $c_0^{(r)} = \langle \chi_0^{(r)} \rangle$  represent the initial volume fractions of the given phases. Furthermore,  $\mathcal{K}$  denotes the set of kinematically admissible deformation gradients:

$$\mathcal{K}(\bar{\mathbf{F}}) = \left\{ \mathbf{F} \mid \exists \mathbf{x} = \mathbf{x}(\mathbf{X}) \text{ with } \mathbf{F} = \frac{\partial \mathbf{x}}{\partial \mathbf{X}}, J > 0, \text{ in } \Omega_0, \mathbf{x} = \bar{\mathbf{F}}\mathbf{X} \text{ on } \partial\Omega_0 \right\}. \quad (6)$$

In physical terms,  $\bar{W}$  represents the average elastic energy stored in the composite when subjected to an affine displacement boundary condition that is consistent with  $\langle \mathbf{F} \rangle = \bar{\mathbf{F}}$ . It is also interesting to remark that, by virtue of definition (5) and the assumed objectivity of  $W$ ,  $\bar{W}$  is an *objective* scalar function of the macroscopic deformation gradient  $\bar{\mathbf{F}}$ .

At this stage, it is important to realize that—because of the non-convexity of  $W$  on  $\mathbf{F}$ —the solution (assuming that it exists) of the Euler–Lagrange equations associated with the variational problem (5) need not be unique. Physically, this corresponds to the possible development of *instabilities* in the composite under sufficiently large deformations. Following Triantafyllidis and co-workers (see, e.g., Geymonat et al., 1993; Triantafyllidis et al., 2006), it is useful to make the distinction between “microscopic” instabilities, that is, instabilities with wavelengths that are small compared to the size of the specimen, and “macroscopic” instabilities, that is, instabilities with wavelengths comparable to the size of the specimen. The computation of microscopic instabilities is, in general, a very difficult problem, especially for composites with *random* microstructures. On the other hand, as explained in more detail below, the computation of macroscopic instabilities is a relatively simple matter, since it amounts to detecting the loss of strong ellipticity of the effective stored-energy function of the material (Geymonat et al., 1993). Hence, in view of the difficulties associated with the computation of microscopic instabilities, we do not attempt here to solve the minimization problem (5), but instead, we adopt a more pragmatic approach. By assuming—for consistency with the classical theory of linear elasticity—that  $W^{(r)}(\mathbf{F}) = \frac{1}{2} \boldsymbol{\varepsilon} \cdot \mathbf{L}_0^{(r)} \boldsymbol{\varepsilon} + o(\boldsymbol{\varepsilon}^3)$  as  $\mathbf{F} \rightarrow \mathbf{I}$ , where  $\boldsymbol{\varepsilon}$  denotes the infinitesimal strain tensor and  $\mathbf{L}_0^{(r)}$  are positive-definite, constant, fourth-order tensors, it is expected that, at least in a neighborhood of  $\bar{\mathbf{F}} = \mathbf{I}$ , the solution of the Euler–Lagrange equations associated with the variational problem (5) is unique, and gives the minimum energy. As the deformation progresses into the finite-deformation regime, the composite may reach a point at which this “principal” solution bifurcates into different energy solutions. This point corresponds to the onset of an *instability*, beyond which the applicability of the principal solution becomes questionable. However, it is still possible to extract useful information from the principal solution by computing the associated macroscopic instabilities from the loss of strong ellipticity of the homogenized behavior. In practice, this

means that we will estimate the effective stored-energy function (5) by means of the *stationary* variational statement:

$$\widehat{W}(\bar{\mathbf{F}}) = \text{stat}_{\mathbf{F} \in \mathcal{X}(\bar{\mathbf{F}})} \sum_{r=1}^2 c_0^{(r)} \langle W^{(r)}(\mathbf{F}) \rangle^{(r)}, \quad (7)$$

where it is emphasized that the energy is evaluated at the above-described principal solution of the relevant Euler–Lagrange equations. In addition, we will estimate the onset of macroscopic instabilities from the loss of strong ellipticity of  $\widehat{W}$ , that is, whenever the inequality<sup>3</sup>

$$\widehat{B}(\bar{\mathbf{F}}) = \min_{\|\mathbf{m}\|=\|\mathbf{N}\|=1} \{m_i N_j \widehat{\mathcal{L}}_{ijkl}(\bar{\mathbf{F}}) m_k N_l\} > 0, \quad (8)$$

ceases to hold true. In this last expression,  $\widehat{\mathcal{L}}(\bar{\mathbf{F}}) = \partial^2 \widehat{W}(\bar{\mathbf{F}}) / \partial \bar{\mathbf{F}}^2$  is the effective incremental elastic modulus characterizing the overall incremental response of the composite. Note that loss of strong ellipticity, as detected from failure of condition (8), provides the critical deformation gradients,  $\bar{\mathbf{F}}_{\text{crit}}$ , at which the homogenized material becomes macroscopically unstable, as well as the pairs of unit vectors  $\mathbf{N}$  and  $\mathbf{m}$  for which these macroscopic instabilities occur. Here,  $\mathbf{N}$  denotes the normal (in the undeformed configuration) to the surface of a weak or strong discontinuity of the deformation field, whereas  $\mathbf{m}$  characterizes the type of deformation associated with such a discontinuity (see, e.g., Knowles and Sternberg, 1975).

Following up on the preceding formulation, the main purpose of the present work is to generate an estimate for the effective stored-energy function (7) for oriented TPEs with lamellar morphology. A second aim of this work is to establish the possible development of macroscopic instabilities in these materials, as well as to provide estimates for the evolution of suitably identified microstructural variables. These objectives are accomplished here by means of the tangent second-order homogenization method (Ponte Castañeda and Tiberio, 2000). The main concept behind this method is the construction of suitable variational principles making use of the idea of a “linear comparison composite” (LCC) with the same microstructure as the hyperelastic composite (i.e., the same  $\chi_0^{(r)}$ ). For completeness, in the next subsection, we recall the main results of the tangent second-order theory that are relevant for our purposes. The interested reader is referred to Ponte Castañeda and Tiberio (2000) for a detailed derivation of this technique.

### 3.1. Tangent second-order variational method

By making use of the general results of Ponte Castañeda and Tiberio (2000), the tangent second-order estimate for the effective stored-energy function (7) of a hyperelastic composite, made up of two phases characterized by the stored-energy functions  $W^{(1)}$  and  $W^{(2)}$  with corresponding initial volume fractions  $c_0^{(1)}$  and  $c_0^{(2)}$ , reads as

$$\widehat{W}(\bar{\mathbf{F}}) = \sum_{r=1}^2 c_0^{(r)} \left[ W^{(r)}(\bar{\mathbf{F}}^{(r)}) + \frac{1}{2} \mathcal{S}^{(r)}(\bar{\mathbf{F}}^{(r)}) \cdot (\bar{\mathbf{F}} - \bar{\mathbf{F}}^{(r)}) \right]. \quad (9)$$

In this relation,  $\bar{\mathbf{F}}^{(r)}$  denotes the average deformation gradient of phase  $r$  in an LCC with the *same microstructure*—in the undeformed configuration—as the original hyperelastic composite, and with *local* stored-energy functions given by

$$W_T^{(r)}(\mathbf{F}) = W^{(r)}(\bar{\mathbf{F}}^{(r)}) + \mathcal{S}^{(r)}(\bar{\mathbf{F}}^{(r)}) \cdot (\mathbf{F} - \bar{\mathbf{F}}^{(r)}) + \frac{1}{2} (\mathbf{F} - \bar{\mathbf{F}}^{(r)}) \cdot \mathcal{L}^{(r)}(\bar{\mathbf{F}}^{(r)}) (\mathbf{F} - \bar{\mathbf{F}}^{(r)}). \quad (10)$$

In the above expressions, the notations  $\mathcal{S}^{(r)}(\cdot) = \partial W^{(r)}(\cdot) / \partial \mathbf{F}$  and  $\mathcal{L}^{(r)}(\cdot) = \partial^2 W^{(r)}(\cdot) / \partial \mathbf{F}^2$  have been introduced for convenience.

The *overall* stored-energy function  $\widehat{W}_T$  for the above-defined LCC may be expressed (see, e.g., Lopez-Pamies and Ponte Castañeda, 2006a) as follows:

$$\widehat{W}_T(\bar{\mathbf{F}}) = \tilde{\mathbf{g}} + \tilde{\mathbf{T}} \cdot \bar{\mathbf{F}} + \frac{1}{2} \tilde{\mathbf{F}} \cdot \tilde{\mathbf{L}} \bar{\mathbf{F}}, \quad (11)$$

where  $\tilde{\mathbf{g}} = \bar{\mathbf{g}} + \frac{1}{2} (\Delta \mathcal{L})^{-1} \Delta \mathbf{T} \cdot (\tilde{\mathbf{L}} - \overline{\mathcal{L}}) (\Delta \mathcal{L})^{-1} \Delta \mathbf{T}$ ,  $\tilde{\mathbf{T}} = \bar{\mathbf{T}} + (\tilde{\mathbf{L}} - \overline{\mathcal{L}}) (\Delta \mathcal{L})^{-1} \Delta \mathbf{T}$  are *effective* quantities depending on  $\tilde{\mathbf{L}}$ , which stands for the effective modulus tensor of the LCC. Also, in the above expressions,  $\mathbf{g}^{(r)} = W^{(r)}(\bar{\mathbf{F}}^{(r)}) - \mathbf{T}^{(r)} \cdot \bar{\mathbf{F}}^{(r)} - \frac{1}{2} \bar{\mathbf{F}}^{(r)} \cdot \mathcal{L}^{(r)}(\bar{\mathbf{F}}^{(r)}) \bar{\mathbf{F}}^{(r)}$ ,  $\mathbf{T}^{(r)} = \mathcal{S}^{(r)}(\bar{\mathbf{F}}^{(r)}) - \mathcal{L}^{(r)}(\bar{\mathbf{F}}^{(r)}) \bar{\mathbf{F}}^{(r)}$  ( $r = 1, 2$ ), and  $\Delta \mathcal{L} = \mathcal{L}^{(1)}(\bar{\mathbf{F}}^{(1)}) - \mathcal{L}^{(2)}(\bar{\mathbf{F}}^{(2)})$ ,  $\Delta \mathbf{T} = \mathbf{T}^{(1)} - \mathbf{T}^{(2)}$ . Furthermore,  $\bar{\mathbf{g}} = c_0^{(1)} \mathbf{g}^{(1)} + c_0^{(2)} \mathbf{g}^{(2)}$ ,  $\bar{\mathbf{T}} = c_0^{(1)} \mathbf{T}^{(1)} + c_0^{(2)} \mathbf{T}^{(2)}$ , and  $\overline{\mathcal{L}} = c_0^{(1)} \mathcal{L}^{(1)}(\bar{\mathbf{F}}^{(1)}) + c_0^{(2)} \mathcal{L}^{(2)}(\bar{\mathbf{F}}^{(2)})$ .

The average deformation gradients  $\bar{\mathbf{F}}^{(1)}$  and  $\bar{\mathbf{F}}^{(2)}$ —needed in the computation of the tangent second-order estimate (9)—can be expediently computed from knowledge of the effective stored-energy function (11) (see, e.g., Ponte Castañeda and Tiberio, 2000, for a derivation). The final expressions may be cast as

$$\bar{\mathbf{F}}^{(1)} = \bar{\mathbf{F}} + \frac{1}{c_0^{(1)}} (\Delta \mathcal{L})^{-1} (\tilde{\mathbf{L}} - \overline{\mathcal{L}}) (\Delta \mathcal{L})^{-1} [\mathcal{S}^{(1)}(\bar{\mathbf{F}}^{(1)}) - \mathcal{S}^{(2)}(\bar{\mathbf{F}}^{(2)}) + \mathcal{L}^{(1)}(\bar{\mathbf{F}}^{(1)}) (\bar{\mathbf{F}} - \bar{\mathbf{F}}^{(1)}) - \mathcal{L}^{(2)}(\bar{\mathbf{F}}^{(2)}) (\bar{\mathbf{F}} - \bar{\mathbf{F}}^{(2)})] \quad (12)$$

and

$$\bar{\mathbf{F}}^{(2)} = \frac{1}{c_0^{(2)}} \bar{\mathbf{F}} - \frac{c_0^{(1)}}{c_0^{(2)}} \bar{\mathbf{F}}^{(1)}. \quad (13)$$

<sup>3</sup> Here and subsequently, unless otherwise indicated, lowercase Latin indices range from 1 to 3 and the usual summation convention is employed.

In connection with the above relations, it is useful to note that Eq. (13) provides an *explicit* expression for  $\bar{\mathbf{F}}^{(2)}$  in terms of  $\bar{\mathbf{F}}$  and  $\bar{\mathbf{F}}^{(1)}$ . This allows relation (12) to be considered as an *implicit* tensorial equation for  $\bar{\mathbf{F}}^{(1)}$ . In this regard, it is also important to remark that Eq. (12) depends directly on the effective modulus tensor  $\tilde{\mathbf{L}}$  of the relevant LCC. Explicit expressions for  $\tilde{\mathbf{L}}$  will be provided in the sequel.

#### 4. Effective behavior of NSC lamellar TPEs

In this section, we turn our attention to *highly oriented, NSC* lamellar morphologies. In particular, based on the experimental evidence presented in Section 2, we consider oriented TPEs to be *granular* systems whose grains are made up of the same, perfect, lamellar structure (SC) with *slightly different* lamination directions (crystal orientations), as illustrated schematically in Fig. 4.

More specifically, NSC TPEs are viewed as materials with heterogeneities at two different scales. These scales are characterized by three different lengths: (i) the repeat length of the perfect lamellar structure  $L_0$ , (ii) the size of the grains  $B$ , and (iii) the characteristic size  $A$  of a sufficiently large specimen  $\Omega_0$ , which are assumed to be well separated in the sense that  $L_0 \ll B \ll A$  (see Fig. 4). In view of this last string of inequalities, the effective properties of NSC TPEs can be obtained by a two-scale homogenization procedure that may be split into two successive steps. The first step consists in the homogenization of the perfectly oriented, SC TPE in order to generate the effective behavior of the individual grains. The second step—to be described in this section—consists of the homogenization of the granular structure.

As a first approximation, we make the simplifying assumption that there are only two distinct initial lamination directions—or crystal orientations—in the granular material. (Recall from Section 2 that in reality there is a continuous distribution of slightly different lamination directions.) They are characterized by the unit vectors  $\mathbf{N}^{(1)}$  and  $\mathbf{N}^{(2)}$ , and have corresponding initial volume fractions  $c_0^{(1)}$  and  $c_0^{(2)}$  (see Fig. 4). We further assume that these lamination directions are distributed *randomly* with *ellipsoidal symmetry* in the undeformed configuration (Willis, 1977). For ease of notation, the stored-energy function characterizing the constitutive behavior associated with the lamination direction  $\mathbf{N}^{(1)}$  is denoted by  $W^{(1)}$ . Its constitutive behavior is determined by making use of the single laminate theory (Triantafyllidis and Maker, 1985; Triantafyllidis and Nestorvić, 2005; Lopez-Pamies and Ponte Castañeda, 2008). Similarly,  $W^{(2)}$  denotes the stored-energy function associated with the lamination direction  $\mathbf{N}^{(2)}$ . Note that in terms of  $W^{(1)}$ ,  $W^{(2)}$  can be written as

$$W^{(2)}(\mathbf{F}) = W^{(1)}(\mathbf{F}\mathbf{Q}), \quad (14)$$

where the proper orthogonal tensor  $\mathbf{Q}$ —defined by  $\mathbf{N}^{(2)} = \mathbf{Q}\mathbf{N}^{(1)}$ —serves to measure the “heterogeneity contrast” between the two crystal orientations. In this connection, it is useful to define  $\delta\mathbf{Q} = \mathbf{Q} - \mathbf{I}$  as the tensorial parameter that quantifies the heterogeneity in the granular material. Accordingly, at  $\delta\mathbf{Q} = \mathbf{0}$  the material reduces to a homogeneous SC, and as  $\delta\mathbf{Q}$  deviates from zero, the material becomes more heterogeneous.

In this section, the effective behavior of the above-defined granular composite is estimated by means of the tangent second-order homogenization theory. As already pointed out in the Introduction, this method has the distinguishing feature of being exact to second order in the heterogeneity contrast (i.e., to  $O(\delta\mathbf{Q}^2)$ ). The limit  $\delta\mathbf{Q} \rightarrow \mathbf{0}$  is of particular interest in the present context, since the focus of this work is precisely on NSC microstructures, namely, on small  $\delta\mathbf{Q}$ . In this regard, we have included in Appendix A the *exact asymptotic results* to second order in  $\delta\mathbf{Q}$ . We conclude finally by identifying certain relevant microstructural variables and providing equations for their evolution along a given loading path.

##### 4.1. Tangent second-order homogenization estimates

By making use of the general results of Section 3.1, the tangent second-order estimate for the effective stored-energy function  $\hat{W}$  of a granular material, made up of two crystal orientations characterized by the stored-energy functions  $W^{(1)}(\mathbf{F})$

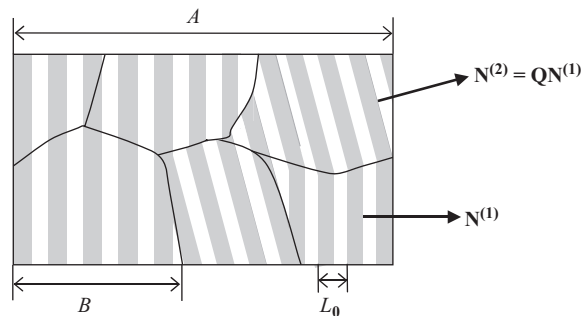


**Fig. 4.** Schematic of a highly oriented, near-single-crystal lamellar TPE in the undeformed configuration with two distinct lamination directions:  $\mathbf{N}^{(1)}$  and  $\mathbf{N}^{(2)} = \mathbf{Q}\mathbf{N}^{(1)}$ , where  $\mathbf{Q}$  is a proper orthogonal tensor. The characteristic length of the specimen  $A$ , the grain size  $B$ , and the repeat length  $L_0$  are assumed to be well separated in the sense that  $L_0 \ll B \ll A$ .

and  $W^{(2)}(\mathbf{F}) = W^{(1)}(\mathbf{F}\mathbf{Q})$  with corresponding initial volume fractions  $c_0^{(1)}$  and  $c_0^{(2)}$ , may be obtained from relation (9). In this expression, it is recalled that the variables  $\bar{\mathbf{F}}^{(r)}$ —which are ultimately functions of the applied loading  $\bar{\mathbf{F}}$ , the material properties of the phases, and the initial microstructure—stand for the average deformation gradients in an optimally selected LCC with the same microstructure (in the undeformed configuration) as the original nonlinear composite. More specifically,  $\bar{\mathbf{F}}^{(1)}$  and  $\bar{\mathbf{F}}^{(2)}$  must be determined from relations (12) and (13), respectively. As discussed in Section 3.1, these relations depend directly on the effective modulus tensor  $\bar{\mathbf{L}}$  of the relevant LCC. In this section, in view of the “granular” type of microstructures of interest, use is made of the following *self-consistent* estimate (Willis, 1977) for the effective modulus tensor of the LCC:

$$\tilde{\mathbf{L}} = \mathcal{L}^{(1)}(\bar{\mathbf{F}}^{(1)}) + c_0^{(2)}[\tilde{\mathbf{P}} - c_0^{(1)}(\tilde{\mathbf{L}} - \mathcal{L}^{(2)}(\bar{\mathbf{F}}^{(2)}))^{-1}]^{-1}, \tag{15}$$

where the microstructural tensor  $\tilde{\mathbf{P}}$  is given by

$$\tilde{\mathbf{P}} = \frac{1}{4\pi \det \mathbf{Z}_0} \int_{\|\xi\|=1} \|\mathbf{Z}_0^{-1}\xi\|^{-3} \tilde{\mathbf{H}}(\xi) dS. \tag{16}$$

In this relation,  $\tilde{H}_{ijkl}(\xi) = \tilde{K}_{ik}^{-1} \xi_j \xi_l$  with  $\tilde{K}_{ik} = \tilde{L}_{ijkl} \xi_j \xi_l$ . Moreover, following Willis (1977), the symmetric second-order tensor  $\mathbf{Z}_0$  serves to characterize the “shape” and “orientation” of the assumed ellipsoidal distribution of the two laminations directions,  $\mathbf{N}^{(1)}$  and  $\mathbf{N}^{(2)}$ , in the undeformed configuration. In this regard, it is fitting to recall that the estimate (15) contains information about the one- and two-point statistics describing the initial microstructure of the composite (Willis, 1977). From a computational point of view, it is also important to remark that expression (15) constitutes an *implicit* equation for  $\tilde{\mathbf{L}}$  that must, in general, be determined numerically.

*Summary of the 3D constitutive model:* In summary, by exploiting the *explicit* form (13) for  $\bar{\mathbf{F}}^{(2)}$ , Eqs. (12) and (15) can be seen to reduce to a *closed* system of 54 *nonlinear* algebraic equations for the 54 scalar unknowns formed by the nine components of  $\bar{\mathbf{F}}^{(1)}$  and the 45 independent components of  $\tilde{\mathbf{L}}$ , which in general must be solved numerically. Having computed all the components of  $\bar{\mathbf{F}}^{(1)}$  and  $\tilde{\mathbf{L}}$  for a given loading ( $\bar{\mathbf{F}}$ ), given phases ( $W^{(1)}$  and  $W^{(2)}$ ), and given initial microstructure ( $c_0^{(1)}$ ,  $c_0^{(2)}$ , and  $\mathbf{Z}_0$ ), the tangent second-order estimate (9) for the effective stored-energy function  $\hat{W}$  of NSC TPEs can be readily obtained. It should be emphasized that these second-order estimates are valid for arbitrary heterogeneity contrast, or equivalently, for any value of  $\delta\mathbf{Q}$ . However, the main interest of this work is for NSC TPEs with  $\delta\mathbf{Q}$  small. For this reason, the limit as  $\delta\mathbf{Q} \rightarrow \mathbf{0}$  of the second-order estimate (9) is considered in Appendix A, and the asymptotic expression (43)—exact to second order in  $\delta\mathbf{Q}$ —is derived.

#### 4.2. Microstructure evolution

The preceding subsection has provided an estimate for the effective mechanical properties of NSC TPEs. In this subsection, with the aim of gaining a more fundamental understanding on the behavior of these materials, we identify relevant microstructural variables and provide expressions for their evolution along a given macroscopic loading path.

It is plain that under finite deformations the size, shape, orientation, and distribution of the underlying grains in the type of granular materials of interest here will not remain fixed, but will instead evolve at every step of the deformation. For brevity, however, these issues will be considered elsewhere. In this work, we will focus on the evolution of the lamellar structures within the grains. Thus, the relevant microstructural variables are identified here as: (i) the *average repeat lengths*,  $L^{(1)}$  and  $L^{(2)}$  and (ii) the *average lamination directions*,  $\mathbf{n}^{(1)}$  and  $\mathbf{n}^{(2)}$ , in the two families of grains—with initial lamination directions  $\mathbf{N}^{(1)}$  and  $\mathbf{N}^{(2)}$ —in the deformed configuration (see Fig. 5). More precisely, the relevant microstructural variables are (see Appendix B in Lopez-Pamies and Ponte Castañeda, 2008 for a derivation of these expressions):

$$L^{(r)} = \frac{1}{|\Omega_0^{(r)}|} \int_{\Omega_0^{(r)}} \|\mathbf{F}^{-T}(\mathbf{X})\mathbf{N}^{(r)}\|^{-1} L_0 d\mathbf{X} \tag{17}$$

and

$$\mathbf{n}^{(r)} = \frac{1}{|\Omega_0^{(r)}|} \int_{\Omega_0^{(r)}} \|\mathbf{F}^{-T}(\mathbf{X})\mathbf{N}^{(r)}\|^{-1} \mathbf{F}^{-T}(\mathbf{X})\mathbf{N}^{(r)} d\mathbf{X}. \tag{18}$$

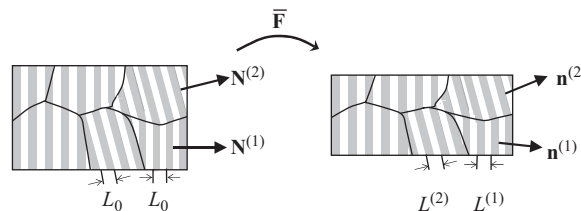


**Fig. 5.** Schematic representation of the evolution of the repeat length,  $L_0$ , and direction of laminations,  $\mathbf{N}^{(1)}$  and  $\mathbf{N}^{(2)}$ , in the two underlying crystal orientations along a given macroscopic loading path  $\bar{\mathbf{F}}$ .

In general, the exact computation of expressions (17) and (18) is an extremely difficult task. However, they may be readily approximated by

$$L^{(r)} = \|\bar{\mathbf{F}}^{(r)-T} \mathbf{N}^{(r)}\|^{-1} L_0 \quad (19)$$

and

$$\mathbf{n}^{(r)} = \|\bar{\mathbf{F}}^{(r)-T} \mathbf{N}^{(r)}\|^{-1} \bar{\mathbf{F}}^{(r)-T} \mathbf{N}^{(r)}, \quad (20)$$

where it is recalled that  $\bar{\mathbf{F}}^{(1)}$  and  $\bar{\mathbf{F}}^{(2)}$ , which stand for the phase average deformation gradients in the relevant LCC, are given by expressions (12) and (13), respectively. In this connection, it is relevant to emphasize that relations (19) and (20) coincide with expressions (17) and (18), respectively, to first order in the heterogeneity contrast (i.e., to  $O(\delta\mathbf{Q})$ ). Moreover, as  $\delta\mathbf{Q}$  deviates from zero far beyond order  $\delta\mathbf{Q}$ , the accuracy of the approximations (19) and (20) is expected to worsen.

## 5. A plane-strain idealization of the problem

With the objective of gaining insight into the properties of the above-proposed constitutive model, in this section we further idealize the problem described in the previous section keeping only the features that are essential to describe at least qualitatively the observed experimental results. More detailed comparisons of the above-developed theoretical results with macroscopic stress–strain and *in situ* SAXS measurements in SBS triblock-copolymer films subjected to various types of loading conditions will be provided elsewhere.

Thus, we study here the problem of *plane-strain loading* (in the  $\mathbf{e}_1$ – $\mathbf{e}_2$  plane):  $\bar{\mathbf{F}} = \bar{F}_{11}\mathbf{e}_1 \otimes \mathbf{e}_1 + \bar{F}_{12}\mathbf{e}_1 \otimes \mathbf{e}_2 + \bar{F}_{21}\mathbf{e}_2 \otimes \mathbf{e}_1 + \bar{F}_{22}\mathbf{e}_2 \otimes \mathbf{e}_2 + \mathbf{e}_3 \otimes \mathbf{e}_3$ , of a subclass of the general type of granular material systems described in Section 4. More specifically, we consider that the two different crystal orientations—with initial volume fractions  $c_0^{(1)}$  and  $c_0^{(2)} (= 1 - c_0^{(1)})$ —are characterized by the *in-plane* unit vectors  $\mathbf{N}^{(1)} = \mathbf{e}_1$  and  $\mathbf{N}^{(2)} = \mathbf{Q}\mathbf{N}^{(1)} = \cos\phi_0^{(2)}\mathbf{e}_1 + \sin\phi_0^{(2)}\mathbf{e}_2$ , so that the “crystal” heterogeneity contrast is determined by the small parameter  $\delta\mathbf{Q} = (\cos\phi_0^{(2)} - 1)(\mathbf{e}_1 \otimes \mathbf{e}_1 + \mathbf{e}_2 \otimes \mathbf{e}_2) + \sin\phi_0^{(2)}(\mathbf{e}_2 \otimes \mathbf{e}_1 - \mathbf{e}_1 \otimes \mathbf{e}_2)$ . Moreover, the spatial distribution of the lamination directions  $\mathbf{N}^{(1)}$  and  $\mathbf{N}^{(2)}$  is considered to be *random* and *transversely isotropic* (with symmetry axis  $\mathbf{e}_3$ ) in the undeformed configuration. Making contact with the microstructural tensor (16), this means that  $Z_0 = \text{diag}(1, 1, \varepsilon)$ , where  $\varepsilon \rightarrow 0$  (see, e.g., Willis, 1982, for further details). Finally, at the smaller length scale within the underlying grains, we assume that the perfect lamellar structures are made up of Neo-Hookean phases—denoted here by superscripts “B” and “S” for clarity of notation—with local stored-energy functions:

$$W^{(B)}(\mathbf{F}) = \frac{\mu^{(B)}}{2}(\mathbf{F} \cdot \mathbf{F} - 3) - \mu^{(B)} \ln(\det \mathbf{F}) + \left(\frac{\kappa^{(B)}}{2} - \frac{\mu^{(B)}}{3}\right)(\det \mathbf{F} - 1)^2, \\ W^{(S)}(\mathbf{F}) = tW^{(B)}(\mathbf{F}) \quad (21)$$

and corresponding initial volume fractions  $c_0^{(B)}$  and  $c_0^{(S)} (= 1 - c_0^{(B)})$ . In these expressions,  $\mu^{(B)}$  and  $\kappa^{(B)}$  denote the shear and bulk moduli of phase B at zero strain, while the parameter  $t$  quantifies the “layer” contrast between phases B and S.

In order to carry out the specialization of the tangent second-order estimate (9) to the above-stated model problem, first, it is useful to establish the specific forms for the stored-energy functions  $W^{(r)}(\bar{\mathbf{F}}^{(r)})$ , stresses  $\mathcal{S}^{(r)}(\bar{\mathbf{F}}^{(r)})$ , and incremental modulus tensors  $\mathcal{L}^{(r)}(\bar{\mathbf{F}}^{(r)})$  ( $r = 1, 2$ ) associated, respectively, grains with the two initial lamination directions  $\mathbf{N}^{(1)}$  and  $\mathbf{N}^{(2)}$ . Making use of the results of Lopez-Pamies and Ponte Castañeda (2008), we have that

$$W^{(1)}(\bar{\mathbf{F}}^{(1)}) = c_0^{(B)}W^{(B)}(\bar{\mathbf{F}}^{(B)}) + c_0^{(S)}W^{(S)}(\bar{\mathbf{F}}^{(S)}), \quad (22)$$

$$\mathcal{S}^{(1)}(\bar{\mathbf{F}}^{(1)}) = c_0^{(B)}\mathcal{S}^{(B)}(\bar{\mathbf{F}}^{(B)}) + c_0^{(S)}\mathcal{S}^{(S)}(\bar{\mathbf{F}}^{(S)}), \quad (23)$$

$$\mathcal{L}^{(1)}(\bar{\mathbf{F}}^{(1)}) = \mathcal{L}^{(B)}(\bar{\mathbf{F}}^{(B)}) + c_0^{(S)}[c_0^{(B)}\mathbf{H}^{(1)} - (\mathcal{L}^{(B)}(\bar{\mathbf{F}}^{(B)}) - \mathcal{L}^{(S)}(\bar{\mathbf{F}}^{(S)}))^{-1}]^{-1}, \quad (24)$$

where  $H_{ijkl}^{(1)} = (K_{ik}^{(B)}(\bar{\mathbf{F}}^{(B)}))^{-1}N_j^{(1)}N_l^{(1)}$ , with  $K_{ik}^{(B)}(\bar{\mathbf{F}}^{(B)}) = \mathcal{L}_{ipkq}^{(B)}(\bar{\mathbf{F}}^{(B)})N_p^{(1)}N_q^{(1)}$  and  $\bar{\mathbf{F}}^{(S)} = 1/c_0^{(S)}\bar{\mathbf{F}}^{(1)} - c_0^{(B)}/c_0^{(S)}\bar{\mathbf{F}}^{(B)}$ . Moreover, making use of the rectangular Cartesian basis  $\{\mathbf{e}_i\}$  as the laboratory frame of reference,  $\bar{F}_{m2}^{(B)} = \bar{F}_{m2}^{(1)}$ ,  $\bar{F}_{m3}^{(B)} = \bar{F}_{m3}^{(1)}$  ( $m = 1, 2, 3$ ),  $\bar{F}_{31}^{(B)} = 0$ , and  $\bar{F}_{11}^{(B)}$  and  $\bar{F}_{21}^{(B)}$  are determined by the following two (coupled) equations:

$$\mathcal{L}_{11}^{(B)}(\bar{\mathbf{F}}^{(B)}) - \mathcal{L}_{11}^{(S)}(\bar{\mathbf{F}}^{(S)}) = 0, \quad \mathcal{L}_{21}^{(B)}(\bar{\mathbf{F}}^{(B)}) - \mathcal{L}_{21}^{(S)}(\bar{\mathbf{F}}^{(S)}) = 0, \quad (25)$$

which, although nonlinear, can be solved in *closed form*. Because of their bulkiness, however, the final explicit expressions for  $\bar{F}_{11}^{(B)}$  and  $\bar{F}_{21}^{(B)}$  will not be included here.

Next, we note that the corresponding expressions for  $W^{(2)}(\bar{\mathbf{F}}^{(2)})$ ,  $\mathcal{S}^{(2)}(\bar{\mathbf{F}}^{(2)})$ ,  $\mathcal{L}^{(2)}(\bar{\mathbf{F}}^{(2)})$  can be readily obtained by making use of relations (22)–(24) together with the following conditions:

$$W^{(2)}(\mathbf{F}) = W^{(1)}(\mathbf{F}\mathbf{Q}), \quad \mathcal{S}_{ij}^{(2)}(\mathbf{F}) = \mathcal{S}_{im}^{(1)}(\mathbf{F}\mathbf{Q})Q_{jm}, \quad \mathcal{L}_{ijkl}^{(2)}(\mathbf{F}) = \mathcal{L}_{ipkq}^{(1)}(\mathbf{F}\mathbf{Q})Q_{jp}Q_{lq}, \quad (26)$$

where it is recalled that  $\mathbf{Q} = \cos\phi_0^{(2)}(\mathbf{e}_1 \otimes \mathbf{e}_1 + \mathbf{e}_2 \otimes \mathbf{e}_2) + \sin\phi_0^{(2)}(\mathbf{e}_2 \otimes \mathbf{e}_1 - \mathbf{e}_1 \otimes \mathbf{e}_2) + \mathbf{e}_3 \otimes \mathbf{e}_3$ .

Having established the relevant constitutive relations for both grain orientations in the granular material, we consider next the computation of the average deformation gradients  $\bar{\mathbf{F}}^{(1)}$  and  $\bar{\mathbf{F}}^{(2)}$ , also needed in the estimate (9). As already stated,  $\bar{\mathbf{F}}^{(2)}$  can be simply obtained from the global average condition (13). On the other hand,  $\bar{\mathbf{F}}^{(1)}$  must be determined from the

tensorial equation (12), which contains nine *scalar* equations. For the model problem at hand, it is easy to check that five out of these nine scalar equations are satisfied identically by the choices:

$$\bar{F}_{33}^{(1)} = 1, \quad \bar{F}_{13}^{(1)} = \bar{F}_{31}^{(1)} = \bar{F}_{23}^{(1)} = \bar{F}_{32}^{(1)} = 0, \quad (27)$$

while the remaining four equations for the four in-plane components  $\bar{F}_{11}^{(1)}, \bar{F}_{12}^{(1)}, \bar{F}_{21}^{(1)}, \bar{F}_{22}^{(1)}$  can be compactly written as

$$\bar{F}_{\alpha\beta}^{(1)} = \bar{F}_{\alpha\beta} + \frac{1}{c_0^{(1)}} \Delta \mathcal{L}_{\alpha\beta\gamma\delta}^{-1} (\tilde{L}_{\gamma\delta\zeta\eta} - \overline{\mathcal{L}}_{\gamma\delta\zeta\eta}) \Delta \mathcal{L}_{\zeta\eta\xi\rho}^{-1} [\mathcal{L}_{\xi\rho}^{(1)}(\bar{\mathbf{F}}^{(1)}) - \mathcal{L}_{\xi\rho}^{(2)}(\bar{\mathbf{F}}^{(2)}) + \mathcal{L}_{\xi\rho\tau\nu}^{(1)}(\bar{\mathbf{F}}^{(1)})(\bar{F}_{\tau\nu} - \bar{F}_{\tau\nu}^{(1)}) - \mathcal{L}_{\xi\rho\tau\nu}^{(2)}(\bar{\mathbf{F}}^{(2)})(\bar{F}_{\tau\nu} - \bar{F}_{\tau\nu}^{(2)})]. \quad (28)$$

In this last expression and below, Greek indices range from 1 to 2. In addition, it is recalled that  $\Delta \mathcal{L} = \mathcal{L}^{(1)}(\bar{\mathbf{F}}^{(1)}) - \mathcal{L}^{(2)}(\bar{\mathbf{F}}^{(2)})$  and  $\overline{\mathcal{L}} = c_0^{(1)} \mathcal{L}^{(1)}(\bar{\mathbf{F}}^{(1)}) + c_0^{(2)} \mathcal{L}^{(2)}(\bar{\mathbf{F}}^{(2)})$ , and, by simplifying relation (15), the in-plane components of the self-consistent modulus tensor  $\tilde{\mathbf{L}}$  can be shown to be exponentially determined by the *implicit* relation:

$$\tilde{L}_{\alpha\beta\gamma\delta} = \mathcal{L}_{\alpha\beta\gamma\delta}^{(1)}(\bar{\mathbf{F}}^{(1)}) + c_0^{(2)} [\tilde{P}_{\alpha\beta\gamma\delta} - c_0^{(1)} (\tilde{L}_{\alpha\beta\gamma\delta} - \mathcal{L}_{\alpha\beta\gamma\delta}^{(2)}(\bar{\mathbf{F}}^{(2)}))^{-1}]^{-1}, \quad (29)$$

where

$$\tilde{P}_{\alpha\beta\gamma\delta} = \frac{1}{2\pi} \int_0^{2\pi} (\tilde{L}_{\alpha\tau\gamma\nu} \xi_\tau \xi_\nu)^{-1} \xi_\beta \xi_\delta \, d\theta \quad (30)$$

with  $\xi_1 = \cos \theta$  and  $\xi_2 = \sin \theta$ .

Finally, making contact with the evolution of microstructure, it is also helpful to spell out (for later use) that the average lamination directions in the deformed configuration, as determined by relation (20), reduce to the *in-plane* unit vectors:

$$n_i^{(r)} = (\cos \phi^{(r)}, \sin \phi^{(r)}, 0)^T \quad (31)$$

( $r = 1, 2$ ), where  $\phi^{(1)} = \tan^{-1}(-\bar{F}_{12}^{(1)}/\bar{F}_{22}^{(1)})$  and  $\phi^{(2)} = \tan^{-1}((\bar{F}_{12}^{(2)} \cos \phi_0^{(2)} - \bar{F}_{11}^{(2)} \sin \phi_0^{(2)})/(\bar{F}_{21}^{(2)} \sin \phi_0^{(2)} - \bar{F}_{22}^{(2)} \cos \phi_0^{(2)}))$ .

*Summary of the 2D constitutive model:* Relations (28) and (29) constitute a closed system of (4 + 10 =) 14 coupled, algebraic equations for the 14 unknowns formed by the four in-plane components of  $\bar{\mathbf{F}}^{(1)}$  ( $\bar{F}_{\alpha\beta}^{(1)}$ ) and the 10 in-plane independent components of  $\tilde{\mathbf{L}}$  ( $\tilde{L}_{\alpha\beta\gamma\delta}$ ). Knowledge of these variables, together with the explicit relations (13) and (27), suffices to compute the tangent second-order estimate (9) for  $\hat{W}$  corresponding to the 2D model problem of interest here. A FORTRAN program has been written for this purpose and is available upon request.

## 6. Results and discussion

In this section, we investigate the strongly anisotropic character of the above-described model for the special case of Neo-Hookean behavior for the “hard” and “soft” phases in the SCs. The objective of this section is to elucidate the critical role that is played by the possible re-orientation of the microstructure, which may introduce enough softening (or stiffening) in the overall response of the material to lead to (or prevent) the development of “macroscopic instabilities” through loss of ellipticity. A more complete description of the response of the oriented TPEs requires consideration of more realistic (than Neo-Hookean) models for both the “soft” and “hard” phases, including plasticity for the latter, but this will be delayed until the next section where a first comparison with experimental results for SBS triblock-copolymer films will be attempted. However, as will be seen in this section, the effect of the microstructure evolution is robust enough to be observed even with the simplest of descriptions for the finite strain response of the two phases.

For simplicity and definiteness, our attention is primarily restricted here to macroscopic *pure shear* loadings of the form

$$\bar{F}_{\alpha\beta} = \begin{bmatrix} \cos \bar{\theta} & -\sin \bar{\theta} \\ \sin \bar{\theta} & \cos \bar{\theta} \end{bmatrix} \begin{bmatrix} \bar{\lambda} & 0 \\ 0 & \bar{\lambda}^{-1} \end{bmatrix} \begin{bmatrix} \cos \bar{\theta} & \sin \bar{\theta} \\ -\sin \bar{\theta} & \cos \bar{\theta} \end{bmatrix}, \quad (32)$$

where  $\bar{\lambda}$  and  $\bar{\lambda}^{-1}$  denote the in-plane macroscopic principal stretches, and  $\bar{\theta}$  serves to characterize the orientation (in the counter-clockwise sense relative to the fixed laboratory frame of reference) of the macroscopic, in-plane, Lagrangian principal axes (i.e., the principal axes of  $\bar{\mathbf{F}}^T \bar{\mathbf{F}}$ ). Results are given for volume fractions,  $c_0^{(1)} = 0.5$ ,  $c_0^{(2)} = 0.6$ , corresponding to typical values for TPEs with lamellar microstructures (see, e.g., Garcia, 2006), while the shear modulus of the soft phase  $\mu^{(B)}$  is normalized to 1. On the other hand, we consider variable values of the bulk modulus  $\kappa^{(B)}$ , “layer contrast”  $t = \mu^{(S)}/\mu^{(B)} = \kappa^{(S)}/\kappa^{(B)}$ , and initial lamination misalignment (or “crystal contrast”)  $\phi_0^{(2)}$ , which provide the sources of nonlinearity and heterogeneity in the material. It is noted that all results are computed up to the point at which the effective behavior is found to lose strong ellipticity (namely, up to the point at which relation (8) ceases to hold true), or truncated at some sufficiently large deformation if no such loss is found. For clarity, the points at which the overall behavior of the material loses strong ellipticity are indicated with the symbol “◦” in the figures.

The results presented here are organized as follows. First, we illustrate results for pure shear at  $\bar{\theta} = 0$ , which corresponds (approximately) to *compression* along the underlying layers within the grains. We then show results for pure shear loading at  $\bar{\theta} = 90^\circ$ , which corresponds (approximately) to *tension* along the layers within the grains. Finally, we show results for pure shear loading at  $\bar{\theta} = 45^\circ$ , corresponding to diagonal loading. These specific choices of loading conditions are particularly useful to illustrate the different mechanisms that govern the overall behavior of oriented TPEs with lamellar

morphology. In addition, they help to bring out the differences between SC (i.e., perfect) and NSC (i.e., imperfect) morphologies, as well as the relative importance of the various material parameters in these systems, in particular, the layer heterogeneity contrast  $t$  and the bulk modulus of the softer phase  $\kappa^{(B)}$ .

*Pure shear loading at  $\bar{\theta} = 0$ :* In Fig. 6, the estimates for the effective response and microstructure evolution of an NSC with misalignment  $\phi_0^{(2)} = 1^\circ$  are compared with the corresponding estimates for a (perfect) SC under pure shear loading at  $\bar{\theta} = 0$ . Results are shown for bulk modulus  $\kappa^{(B)} = 10$  and layer contrast  $t = 10$ , as a function of the macroscopic stretch  $\bar{\lambda}$ . Part (a) shows the macroscopic stress  $\bar{S} = d\bar{W}/d\bar{\lambda}$ , and part (b), the corresponding grain reorientation angles  $\phi^{(1)}$  and  $\phi^{(2)}$ . An immediate observation from Fig. 6(a) is that the effective stress–stretch relationship of the NSC is initially very similar to that of the SC. This is consistent with the fact that the initial morphology of the NSC is but a slight perturbation of that of the SC (i.e.,  $\phi_0^{(2)} = 1^\circ$ ). Note, however, that the stress in the NSC—in contrast to the stress in the SC—undergoes a sudden drop at deformations near loss of strong ellipticity (denoted by “o” in the plots). To understand the source of this sudden drop in the stress, it is useful to consider the corresponding results for the evolution of the underlying microstructure. Thus, Fig. 6(b) shows the evolution of the average angles of rotation of the layers,  $\phi^{(1)}$  and  $\phi^{(2)}$ , of the two families of grains with initial lamination directions  $\mathbf{N}^{(1)}$  and  $\mathbf{N}^{(2)}$  (defined by expression (31)), as functions of the applied stretch  $\bar{\lambda}$ . It is observed in this figure that the layers with initial lamination direction  $\mathbf{N}^{(1)}$  in the NSC rotate clockwise, while the layers with initial lamination direction  $\mathbf{N}^{(2)}$  rotate counter-clockwise. That is, the underlying laminates in the two families of grains rotate in opposite directions. Furthermore, they rotate “faster” with increasing stretch, especially as the loss of strong ellipticity condition is approached. This entails a *geometric softening mechanism* consisting in the reorientation of the layers in each family of grains in a direction that is more favorable to shear, and therefore less stiff than the original orientations. In this connection, it is emphasized that the layered structures in the grains exhibit a “soft” mode of deformation for shear parallel to the layers (like a deck of cards). Thus, the sudden drop in the stress shown in Fig. 6(a) is seen to be a direct consequence of the reorientation of the layers depicted in Fig. 6(b). In addition, it is also important to remark that the rotation of the two families of layers in opposite directions is entirely consistent with the development of “chevron” patterns (or zig-zag structures), which have been observed experimentally in TPEs subjected to tensile loadings in the direction perpendicular to the lamellae (see, e.g., Cohen et al., 2000). By contrast, because of the symmetry, the layers in the (perfect) SC do not rotate at all, but instead remain aligned with the applied loading axes all the way up to the loss of strong ellipticity.

Having analyzed the overall behavior and evolution of microstructure, next we examine the development of instabilities in more detail. This requires consideration of the evolution of the effective incremental moduli, as a function of the applied stretch. Now, Fig. 7(a) clearly shows that the effective incremental behavior of the NSC, as measured by the effective modulus  $\mathcal{L}_{2222}$ , increases initially but then softens dramatically, recovering somewhat, before the material eventually loses ellipticity with  $\mathcal{L}_{1212}$  tending to zero. This loss of ellipticity corresponds to the possible development of a “macroscopic instability” (Geymonat et al., 1993), as will be discussed in more detail in the next paragraph. In this context, it is worth remarking from Fig. 7(a) that the corresponding effective normal modulus  $\mathcal{L}_{2222}$  of the SC—as opposed to that of the NSC—does not decrease at all, but instead increases monotonically up to loss of ellipticity. On the other hand, the effective shear modulus  $\mathcal{L}_{1212}$  of the SC, as well as most of the remaining effective moduli  $\mathcal{L}_{ijkl}$  (not shown here for conciseness), are practically indistinguishable from those of the NSC (although the SC loses ellipticity a little later than the NSC). Thus, the overall responses of the NSC and SC, though similar, exhibit differences that are consistent with the fact that the NSC is an “imperfect” version of the SC.

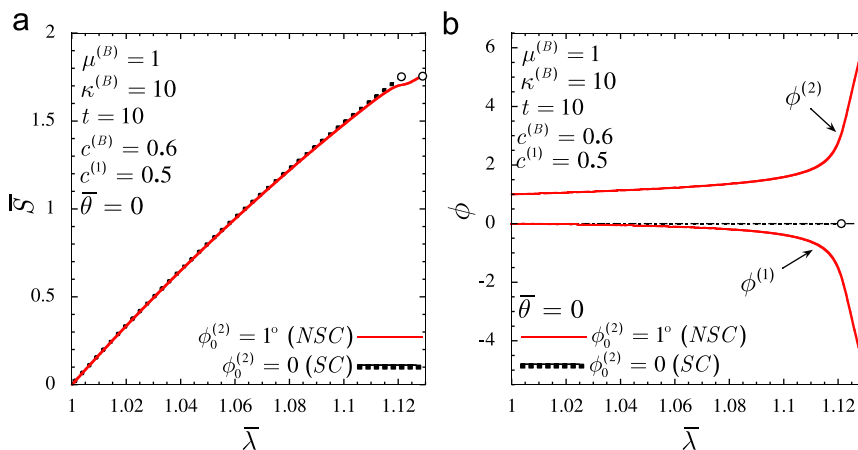


**Fig. 6.** Effective behavior and microstructure evolution in a near-single-crystal (NSC) with  $\phi_0^{(2)} = 1^\circ$ , subjected to pure shear at  $\bar{\theta} = 0$ . The results correspond to bulk modulus  $\kappa^{(B)} = 10$  and layer contrast  $t = 10$ , and are shown as functions of the macroscopic stretch  $\bar{\lambda}$ . (a) The macroscopic stress  $\bar{S} = d\bar{W}/d\bar{\lambda}$ . (b) The evolution of the average angles of rotation of the layers  $\phi^{(1)}$  and  $\phi^{(2)}$ . The corresponding results for a single crystal (SC) have been included (in dotted lines) for comparison purposes.

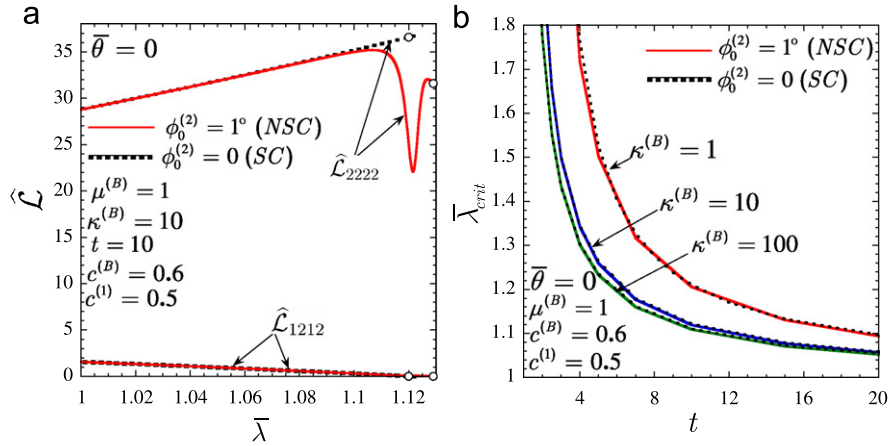


**Fig. 7.** Effective moduli and loss of ellipticity. (a) The effective incremental moduli  $\widehat{\mathcal{L}}_{2222} = \partial^2 \widehat{W} / \partial \bar{F}_{22}^2$  and  $\widehat{\mathcal{L}}_{1212} = \partial^2 \widehat{W} / \partial \bar{F}_{12}^2$ , corresponding to the near-single-crystal (NSC) and single crystal (SC) defined in Fig. 6, as functions of the macroscopic stretch  $\bar{\lambda}$ . (b) The critical stretch,  $\bar{\lambda}_{crit}$ , at which loss of strong ellipticity takes place for various values of the bulk modulus  $\kappa^{(B)}$ , as a function of the layer contrast  $t$ , for pure shear loading at  $\bar{\theta} = 0$  of an NSC with  $\phi_0^{(2)} = 1^\circ$  and an SC.

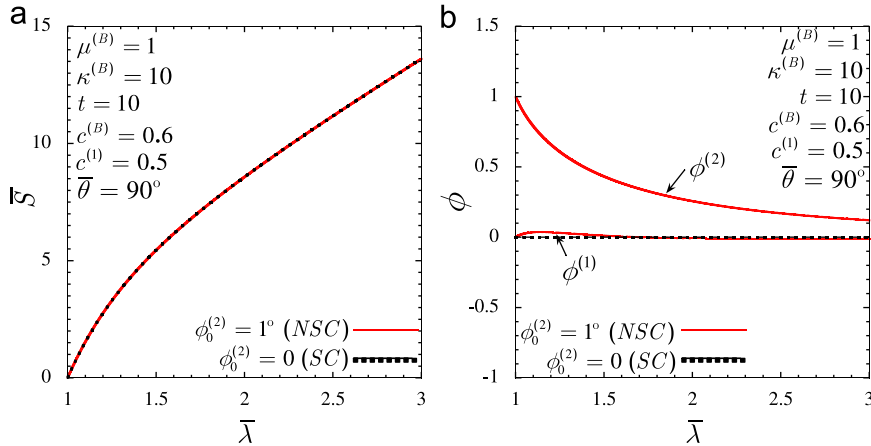


**Fig. 8.** Effective behavior of a near-single-crystal (NSC) with  $\phi_0^{(2)} = 1^\circ$  and a single crystal (SC) subjected to pure shear at  $\bar{\theta} = 90^\circ$ . The results correspond to bulk modulus  $\kappa^{(B)} = 10$  and contrast  $t = 10$ , and are shown as functions of the macroscopic stretch  $\bar{\lambda}$ . (a) The macroscopic stress  $\bar{s} = d\widehat{W}/d\bar{\lambda}$ . (b) The evolution of the average angles of rotation of the layers  $\phi^{(1)}$  and  $\phi^{(2)}$ .

Fig. 7(b) provides results for the critical stretch,  $\bar{\lambda}_{crit}$ , at which the NSC with  $\phi_0^{(2)} = 1^\circ$  and SC first lose strong ellipticity under pure shear at  $\bar{\theta} = 0$  for bulk moduli  $\kappa^{(B)} = 1, 10$ , and  $100$ , as a function of the layer contrast  $t$ . A key observation from this figure is that, under pure shear at  $\bar{\theta} = 0$ , the NSC and SC become macroscopically unstable at smaller stretches  $\bar{\lambda}_{crit}$  for higher values of the contrast  $t$ . In this connection, it is noted that  $\bar{\lambda}_{crit} \rightarrow \infty$  as  $t \rightarrow 1$ . This asymptotic behavior derives from the fact that in the absence of heterogeneity between the lamellae, the material reduces to a homogeneous Neo-Hookean solid (i.e.,  $\widehat{W} = W^{(B)}$ ), which is known to be strongly elliptic for all deformations. On the other hand,  $\bar{\lambda}_{crit} \rightarrow 1$  as  $t \rightarrow \infty$ , so that in the limiting case when the stiffer layers are taken to be rigid, the material is already unstable at zero strain (but *not* at zero stress of course). It is also noted from Fig. 7(b) that the macroscopic stability of the NSC and SC worsens significantly with increasing incompressibility, as measured by the bulk modulus  $\kappa^{(B)}$ . Furthermore, it is interesting to remark that the NSC loses strong ellipticity at very similar (but *not* identical) critical stretches  $\bar{\lambda}_{crit}$  as the SC. In other words, a small perturbation (e.g., here,  $\phi_0^{(2)} = 1^\circ$ ) in the perfect morphology of an SC results in a small perturbation in the critical stretch at which the material becomes macroscopically unstable.

*Pure shear loading at  $\bar{\theta} = 90^\circ$ :* Fig. 8 provides results for the effective response and microstructure evolution of a NSC with  $\phi_0^{(2)} = 1^\circ$  and an SC under pure shear loadings (32) with tensile axis aligned with the layers ( $\bar{\theta} = 90^\circ$ ). Results are shown for bulk modulus  $\kappa^{(B)} = 10$  and layer contrast  $t = 10$ , as a function of the applied stretch  $\bar{\lambda}$ . Parts (a) show the macroscopic stress  $\bar{s} = d\widehat{W}/d\bar{\lambda}$ , and parts (b), the evolution of the average angles of rotation of the layers,  $\phi^{(1)}$  and  $\phi^{(2)}$ . It is observed from Fig. 8(a) that both the NSC and SC materials remain strongly elliptic for the whole range of deformations. In addition, the overall stress–stretch relation of the NSC is practically identical to that of the SC for the *entire range of*

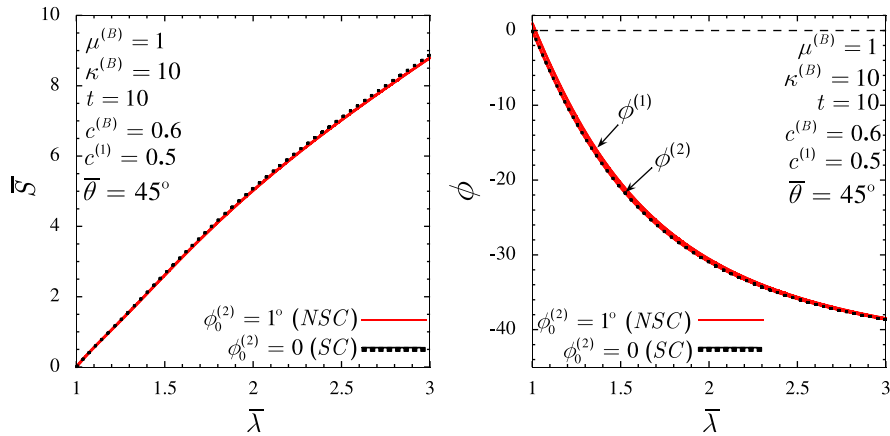


**Fig. 9.** Effective behavior of a near-single-crystal (NSC) with  $\phi_0^{(2)} = 1^\circ$  and a single crystal (SC) subjected to pure shear at  $\bar{\theta} = 45^\circ$ . The results correspond to bulk modulus  $\kappa^{(B)} = 10$  and contrast  $t = 10$ , and are shown as functions of the macroscopic stretch  $\bar{\lambda}$ . (a) The macroscopic stress  $\bar{S} = d\bar{W}/d\bar{\lambda}$ . (b) The evolution of the average angles of rotation of the layers  $\phi^{(1)}$  and  $\phi^{(2)}$ .

deformations considered. Correspondingly, Fig. 8(b) shows that the microstructure evolution for both the NSC and SC are practically identical and—in contrast with the previously studied cases—there is no evidence of the development of any instabilities. More specifically, this figure shows that both families of layers in the NSC, with initial laminations  $\mathbf{N}^{(1)}$  and  $\mathbf{N}^{(2)}$ , rotate (very slightly) in such a manner that they tend to align themselves with the axis of tensile loading (i.e.,  $\phi^{(r)} \rightarrow 0$  as  $\bar{\lambda} \rightarrow \infty$ ), which is the stiffest direction for these materials. On the other hand, the layers in the SC do not rotate at all since they are already perfectly aligned with the tensile axis. Thus, for pure shear at  $\bar{\theta} = 90^\circ$ —as opposed to the preceding case for loading at  $\bar{\theta} = 0^\circ$ —there is hardly any rotation of the layers in the two families of grains for the NSC (or of the layers in the SC), and so there is no softening mechanism which can give rise to a macroscopic instability. The macroscopic response is controlled by the (strongly elliptic) behavior of the phases in this case.

*Pure shear loading at  $\bar{\theta} = 45^\circ$ :* Fig. 9 shows the corresponding results for the effective response and microstructure evolution of the NSC with  $\phi_0^{(2)} = 1^\circ$  and an SC under pure shear loadings (32) with  $\bar{\theta} = 45^\circ$ , as a function of the applied stretch  $\bar{\lambda}$ . It is again observed from Fig. 9(a) that both the NSC and SC materials remain strongly elliptic for the whole range of deformations. In addition, the overall stress–stretch relation of the NSC is practically identical to that of the SC for the entire range of deformations considered. Correspondingly, Fig. 9(b) shows that the microstructure evolution for both the NSC and SC are also practically identical. More specifically, we note from Fig. 9(b) that the layers with initial laminations  $\mathbf{N}^{(1)}$  and  $\mathbf{N}^{(2)}$  in the NSC follow essentially the same rotation as the layers in the SC—namely, they rotate clockwise to align themselves with the axis of tensile loading (i.e.,  $\phi^{(r)} \rightarrow -45^\circ$  as  $\bar{\lambda} \rightarrow \infty$ ). Given the relatively large changes in orientation of the layers, the question then arises as to why no instabilities are observed in this case. The fact is that the reorientation of the layers (past  $45^\circ$ ) actually tends to stiffen the material since the limiting orientation of  $90^\circ$  is actually incrementally stiffer than that of  $45^\circ$  (all other variables being held fixed). This is in contrast with the unstable cases discussed in the context of the results for  $\bar{\theta} = 0^\circ$ , where the reorientation of the layers leads to a “softer” incremental response due to the more favorable orientation for shear loading parallel to the layers (which is the softest deformation mode for these laminated structures). Thus, in conclusion, for pure shear at  $\bar{\theta} = 45^\circ$ , the rotation of the layers in the NSC (and in the SC) provides a stiffening mechanism that actually hinders the possible development of macroscopic instabilities in this case.

## 7. Comparisons with uniaxial tension experiments on SBS films

The preceding section has provided much (qualitative) insight into the constitutive model developed in this work for oriented TPEs with lamellar morphology. To further assess the ability of our models to describe the complex overall mechanical properties of this class of materials, in this section we present comparisons of our theoretical predictions with experimental measurements of the stress–stretch relation in SBS films under uniaxial tensile loading in the parallel, perpendicular, and diagonal directions. As already mentioned, the Neo-Hookean model (21) utilized in Section 5 is clearly too simplistic to characterize the behaviors of the underlying PB and PS constituents in actual SBS films. Therefore, in this section, we will make use of more realistic models for the constitutive behaviors of these elastomeric and glassy phases. However, it is important to emphasize that more thorough quantitative comparisons between the proposed model and experimental results, including microstructure evolution data, would require more precise control on the material microstructure and on the measurements. (Refer to the thesis of Garcia, 2006 for a detailed discussion of the difficulties and sources of experimental error in the measurement of microstructure evolution, and stress and strain in SBS films.) On the other hand, our model, which is based on a homogenization approach, cannot be expected to work beyond the onset of

instabilities. For this reason, we will focus our attention here only to applied stretches up to the onset of any instabilities, which are anticipated to occur based on the results of the previous section, and observed in the experiments, for certain loading conditions. In the sequel, we first describe the experimental results (shown in Fig. 10(a)) and then turn to the discussion of the corresponding theoretical results (shown in Fig. 10(b)).

Fig. 10(a) displays experimental stress–stretch measurements for the class of oriented, lamellar, SBS triblock-copolymer films described in Section 2. The results correspond to *uniaxial tension* at loading angles  $\bar{\theta} = 0, 45^\circ$ , and  $90^\circ$  with respect to the average lamination direction in the undeformed configuration. For small enough deformations, it is observed that the films exhibit a linear stress–stretch response with overall Young’s moduli  $\bar{E}_0 = 29$  MPa,  $\bar{E}_{45^\circ} = 13$  MPa, and  $\bar{E}_{90^\circ} = 260$  MPa, for the tensile loadings at  $\bar{\theta} = 0, 45^\circ$ , and  $90^\circ$ , respectively. The rather interesting anisotropy of this response—which is in accord with the earlier experimental observations of Allan et al. (1991) and Cohen et al. (2000)—can be explained as follows. Physically, uniaxial tension at  $\bar{\theta} = 90^\circ$  corresponds to tensile loading parallel to the layers, which results in the stretching of the hard phase (i.e., the glassy PS) and consequently leads to a stiff overall response. On the other hand, uniaxial tension at  $\bar{\theta} = 45^\circ$  corresponds to shear loading parallel to the layers, which results in the shearing of the soft phase (i.e., the rubbery PB) and consequently in a soft overall response. Finally, uniaxial tension at  $\bar{\theta} = 0$  corresponds to tensile loading perpendicular to the layers, which entails the stretching of the soft phase. However, because of the relatively low compressibility of the soft *rubbery* phase, the resulting Poisson effect provokes a significant stretching of the hard phase as well, and thus the linear response for  $\bar{\theta} = 0$  lies in between those for  $\bar{\theta} = 90^\circ$  and  $45^\circ$ .

Beyond the linear response, the three stress–stretch curves in Fig. 10(a) exhibit a markedly different nonlinear behavior. For uniaxial tension at  $\bar{\theta} = 90^\circ$ , the distinct rollover and actual drop in the macroscopic stress–stretch curve is due to the *plastic yielding* and *breaking* of the PS layers (see Cohen et al., 2000; Garcia, 2006). By contrast, for uniaxial tension at  $\bar{\theta} = 0$ , the distinct (but less strong) rollover in the macroscopic stress–stretch response is *not* due to microscopic plastic yielding, but instead to a *rapid evolution of microstructure*—which ultimately leads to the formation of “chevron” patterns—corresponding to an *elastic instability* (see Cohen et al., 2000; Garcia, 2006). For uniaxial tension at  $\bar{\theta} = 45^\circ$  there is neither microscopic yielding nor elastic instabilities (within the range of deformations considered in Fig. 10(a)). In this case, the nonlinearity in the macroscopic stress–stretch curve is due to the inherent nonlinear elastic behavior of PB at finite deformations, as well as to the smooth rotation of the underlying layers. In this connection, it is also interesting to remark that the overall response at  $\bar{\theta} = 45^\circ$ —which is initially the “softest”—eventually becomes “harder” than the response at  $\bar{\theta} = 0$  beyond approximately  $\bar{\lambda} = 1.34$ .

Before proceeding with the discussion of the theoretical predictions illustrated in Fig. 10(b), we provide some details on the modeling. As pointed out above, the Neo-Hookean behavior utilized in Section 5 is too “crude” to model the actual behavior of the PB and PS phases in SBS films. Accordingly, for the rubbery PB phase, we make use here of the more realistic hyperelastic constitutive relation:

$$W^{(B)}(\mathbf{F}) = \sum_{i=1}^M \frac{\mu^{(i)}}{2\alpha^{(i)}3^{\alpha^{(i)}-1}} [J^{-2/3}I]^{\alpha^{(i)}} - 3^{\alpha^{(i)}}] + \frac{\kappa^{(B)}}{2}(J-1)^2, \quad (33)$$

where  $\mu^{(i)}, \alpha^{(i)}, \kappa^{(B)}$  are material parameters, and it is recalled that  $I = \mathbf{F} \cdot \mathbf{F} = \lambda_1^2 + \lambda_2^2 + \lambda_3^2$  and  $J = \det \mathbf{F} = \lambda_1 \lambda_2 \lambda_3$ . The (compressible) generalized Neo-Hookean stored-energy function (33)—which, similar to the Arruda and Boyce (1993) 8-chain and the Gent (1996) models, is able to account for the typical limiting chain extensibility of elastomers—has been recently shown to accurately describe the behavior of rubber elastic materials over the entire range of deformations

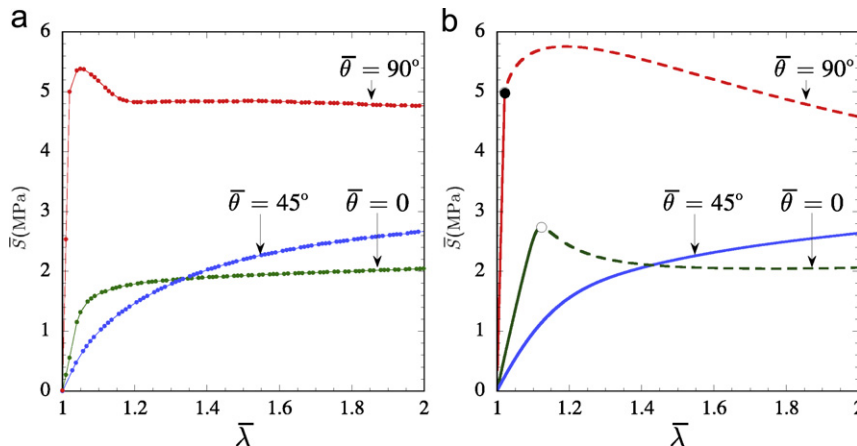


Fig. 10. (a) Experimental stress–stretch results for oriented lamellar SBS triblock-copolymer films subjected to *uniaxial tension* at three different angles  $\bar{\theta}$  with respect to the average initial lamination direction. (b) Theoretical stress–stretch predictions for a near-single crystal SBS triblock-copolymer film with PB phase characterized by the rubber elastic solid (33), and PS phase characterized by the elastic–plastic solid (34).

(Lopez-Pamies, 2008). On the other hand, for the glassy PS phase, we make use of the following piecewise *elastic-plastic* model:

$$W^{(S)}(\mathbf{F}) = \begin{cases} \frac{3\mu^{(S)}}{2}\varepsilon_{\text{eq}}^2 + \frac{\kappa^{(S)}}{2}(\ln J)^2 & \text{if } \varepsilon_{\text{eq}} \leq \varepsilon_Y, \\ \frac{3\mu^{(S)}\varepsilon_Y^2}{m+1}\left(\frac{\varepsilon_{\text{eq}}}{\varepsilon_Y}\right)^{m+1} + \frac{3\mu^{(S)}(m-1)}{2(m+1)}\varepsilon_Y^2 + \frac{\kappa^{(S)}}{2}(\ln J)^2 & \text{if } \varepsilon_{\text{eq}} \geq \varepsilon_Y. \end{cases} \quad (34)$$

In this expression,  $\mu^{(S)}$ ,  $\kappa^{(S)}$ ,  $\varepsilon_Y$ ,  $m$  are material parameters, and  $\varepsilon_{\text{eq}}^2 = \frac{4}{3}(\varepsilon_1^2 + \varepsilon_2^2 + \varepsilon_3^2 - \varepsilon_1\varepsilon_2 - \varepsilon_2\varepsilon_3 - \varepsilon_1\varepsilon_3)$  with  $\varepsilon_i = \ln \lambda_i$  ( $i = 1, 2, 3$ ). Note that Eq. (34) corresponds to a (compressible) finite-deformation version of the elastic–plastic (with power-law hardening) constitutive relation commonly used in deformation theory of plasticity (see, e.g., Abeyaratne and Triantafyllidis, 1981). Thus, the parameters  $\mu^{(S)}$  and  $\kappa^{(S)}$  serve to characterize the shear and bulk modulus of the initially elastic response of the PS, whereas  $\varepsilon_Y$  and  $m$  characterize, respectively, the yield strain and hardening exponent of its plastic response.

Having spelled out the functional form of the constitutive behavior and spacial distribution of the PB and PS phases, we turn to a brief description of how the material parameters for the model are obtained. First, the parameters  $\kappa^{(B)}$ ,  $\mu^{(S)}$ , and  $\kappa^{(S)}$  are computed by fitting the small-strain, linearly elastic data for the three loadings at  $\bar{\theta} = 0, 45^\circ$ , and  $90^\circ$  in Fig. 10(a). Second, the parameters  $\mu^{(i)}$  and  $\alpha^{(i)}$  ( $i = 1, 2, 3$ ) are determined by fitting the large-deformation experimental response at  $\bar{\theta} = 45^\circ$ . Thirdly,  $\varepsilon_Y$  is set to fit the experimentally measured yield stress at  $\bar{\theta} = 90^\circ$ , while the other plastic parameter,  $m$ , is chosen rather arbitrarily, since it does not play a significant role in the results. Finally, the microstructural parameters  $c_0^{(B)}$ ,  $c_0^{(1)}$ , and  $\phi_0^{(2)}$ , as defined in Section 5, are chosen to approximate the SAXS data presented in Section 2. The specific values of all the parameters, as computed for the SBS triblock copolymers of interest here, are listed in Table 1.

Making use of the PB and PS models (33) and (34), together with the material parameters listed in Table 1, in the approach described in Sections 4 and 5 leads to a constitutive model for the macroscopic behavior of oriented SBS triblock-copolymer materials. (A FORTRAN program has been written for this purpose and is available from the authors upon request.) Fig. 10(b) shows the resulting model predictions for *uniaxial tensile* loading at angles  $\bar{\theta} = 0, 45^\circ$ , and  $90^\circ$  with respect to the initial lamination direction  $\mathbf{N}^{(1)} = \mathbf{e}_1$ . Note that in the small-deformation regime, the model results exhibit (of course) behaviors identical to the actual SBS films for all three loading conditions (see Fig. 10(a)). The more interesting large-deformation response is discussed next.

For uniaxial tension at  $\bar{\theta} = 0$ , the model prediction develops a macroscopic (elastic) instability (indicated with the symbol “o” in the plot) at relatively small deformations in a way (discussed in the previous section) that is consistent with the experimentally observed development of “chevron” patterns in the SBS films. It should be noted, however, that the critical stretch at which the model predicts the development of the instability ( $\bar{\lambda}_{\text{crit}}^{\text{th}} = 1.125$ ) is higher than the critical stretch at which the instability is observed to appear in the experiments ( $\bar{\lambda}_{\text{crit}}^{\text{exp}} = 1.07$ ). The nature of this discrepancy is consistent with the fact that  $\bar{\lambda}_{\text{crit}}^{\text{th}}$ , as computed by the loss of strong ellipticity of the macroscopic response, corresponds to an upper bound for any other types of instabilities (Geymonat et al., 1993). For illustrative purposes, the model response has been included in the plot (in dashed lines) for values of  $\bar{\lambda}$  beyond  $\bar{\lambda}_{\text{crit}}^{\text{th}}$ . However, it should be emphasized that the proposed model is expected to be valid at most up to loss of strong ellipticity.

For  $\bar{\theta} = 90^\circ$ , it is seen that the model is able to capture the onset of macroscopic yield (denoted by the symbol “•” in the plot) by keeping track of the local stress levels in the PS layers. The model response after yielding is depicted in the plot with a dashed line to suggest that, in reality, the PS layers are expected to break soon after yielding and therefore a more sophisticated approach than the one used here (e.g., including the formation and growth of a porous phase) would be needed to characterize accurately the response of the films beyond the yielding and breaking of the PS layers.

Finally, for uniaxial tension at  $\bar{\theta} = 45^\circ$ , the theoretical response remains in excellent agreement with the experimental result in the large-deformation regime. More specifically, the experimental results are much smoother and there is no evidence of a macroscopic instability. As already anticipated in the previous section, this interesting phenomenon is due to the fact that while the rotation of the layers for  $\bar{\theta} = 0$  leads to an elastic instability (due to the kinematically induced geometric softening) producing a markedly “softer” response after the onset of the instability, the corresponding rotation of the layers for  $\bar{\theta} = 45^\circ$  actually has a stiffening effect, helping to maintain the macroscopic deformation stable at all times. Moreover, the large rotation of the layers for the  $\bar{\theta} = 45^\circ$  case provides an “accommodating” mechanism allowing these

**Table 1**  
Material parameters

$\kappa^{(B)}$ (MPa)	$\mu^{(1)}$ (MPa)	$\mu^{(2)}$ (MPa)	$\mu^{(3)}$ (MPa)	$\alpha^{(1)}$	$\alpha^{(2)}$	$\alpha^{(3)}$
15	0.0693	1.2038	0.6019	1.5093	0.3510	−4.6650
$\mu^{(S)}$ (MPa)	$\kappa^{(S)}$ (MPa)	$\varepsilon_Y$	$m$	$c_0^{(B)}$	$c_0^{(1)}$	$\phi_0^{(2)}$
213	690	0.0188	0.1	0.58	0.5	1°

materials to undergo large macroscopic stretches without failure. In fact, for very large stretches they can support even larger stresses than the  $\bar{\theta} = 90^\circ$  loading orientation (which is initially the stiffest response).

## 8. Concluding remarks

In this paper, we have developed a constitutive model for the finite-deformation behavior of oriented thermoplastic elastomers with lamellar morphology by means of a two-scale homogenization procedure. In particular, motivated by experimental evidence, we have idealized this class of oriented TPEs as granular systems where the grains are made up of the same, perfect, lamellar structure (single crystal) with different lamination directions (crystal orientations).

With the aim of illustrating the capabilities of the proposed model for the overall response of oriented TPEs, comparisons have been provided with experimental results for the overall stress–strain response of near-single-crystal SBS films under uniaxial tension. These comparisons have revealed a rich range of behaviors for these materials. When loaded in tension along the layer direction, the model shows that the stiffer PS layers in the material yield plastically. In the experiments, this phenomenon is followed by failure of the PS layers and the opening of gaps in the material, which is manifested macroscopically by necking in the damaged region. For the other two loadings considered (tension perpendicular and diagonal to the layer direction), no plastic deformation was observed, but the elastic response of the material was found to be very different. Thus, when loaded perpendicular to the layer direction, the stiff layers in the grains tend to undergo rapid rotations (in opposite directions) leading to the development of a macroscopic (elastic) instability that have been found to be consistent with the formation of “chevron” patterns in experimental results (see, e.g., [Cohen et al., 2000](#)) for these materials. On the other hand, when loaded in tension at  $45^\circ$  with respect to the layer direction, the stiff layers in the grains undergo slow rotations (in the same direction), and the material remains macroscopically stable for all deformations. In conclusion, the possible rotation of the layers has been found to play a crucial role in determining the overall response of the oriented TPEs by providing a geometric softening (or stiffening) mechanism, which can tend to destabilize (or stabilize) the macroscopic response of the material, depending rather sensitively on how the material is loaded.

According to the proposed constitutive model, the possible development of “chevron” patterns for loadings involving compression along the layers is due mainly to the combination of two factors: the existence of (slightly) different lamination directions in the material, and the high heterogeneity contrast between the “hard” and “soft” blocks forming the lamellar nanostructures. In this regard, it should be mentioned that other investigators ([Read et al., 1999](#); [Tzianetopoulou and Boyce, 2004](#)) have simulated (with FEM) the development of “chevron” patterns by considering oriented TPEs as laminates—made up of alternating “hard” and “soft” layers—perturbed with a low-amplitude sinusoidal undulation. This approach is actually not so different from the approach presented in this work. Indeed, the introduction of a low-amplitude waviness also allows these models to account for having a distribution of slightly different lamination directions in the material—which is the essential feature for the formation of “chevron” patterns. However, the approach presented in this paper has the advantage that it can be easily generalized to account for more general distributions of layer orientations in the constituent grains, such as would be present in “unoriented” samples. In fact, the model is general enough to handle variations in the initial “texture” of the sample. This issue is currently being investigated and will be reported elsewhere.

## Acknowledgements

The work of O.L.P. and P.P.C. was supported by Grant DE-FG02-04ER46110 from the Department of Energy (USA). The work of O.L.P., E.C., and J.Y.C. was supported by the Agence Nationale de la Recherche (France), and that of R.G. by CONACYT (Mexico). P.P.C. also acknowledges the support of Grant CMMI-0654063 from the National Science Foundation (USA). Finally, the authors would like to thank J.M. Chenal and V. Racherla for fruitful discussions.

## Appendix A. Asymptotic analysis for $\delta\mathbf{Q} \rightarrow \mathbf{0}$

In this appendix, we present a brief outline of the asymptotic analysis corresponding to the limit of small heterogeneity contrast of the tangent second-order estimate (9) for granular materials made up of two crystal orientations.

We start by assuming that the principal unknown,  $\bar{\mathbf{F}}^{(1)}$ , in the effective stored-energy function (9) admits the following regular asymptotic expansion in the limit as  $\delta\mathbf{Q} \rightarrow \mathbf{0}$ :

$$\bar{\mathbf{F}}^{(1)} = \bar{\mathbf{F}} + \mathbf{A}^{(1)}\delta\mathbf{Q} + \mathbf{A}^{(2)}[\delta\mathbf{Q}, \delta\mathbf{Q}] + O(\delta\mathbf{Q}^3), \quad (35)$$

where  $\mathbf{A}^{(1)}$  and  $\mathbf{A}^{(2)}$  are, respectively, constant fourth- and sixth-order tensors to be determined from the asymptotic analysis that follows. Note that the leading order term in Eq. (35) is given by the macroscopic deformation gradient  $\bar{\mathbf{F}}$ , as suggested by the absence of heterogeneity. Note also that the notation  $\mathbf{A}^{(2)}[\delta\mathbf{Q}, \delta\mathbf{Q}] = A_{ijklmn}^{(2)}\delta Q_{kl}\delta Q_{mn}$  has been utilized in Eq. (35) for convenience.

Having introduced the expansion for  $\bar{\mathbf{F}}^{(1)}$ , it is now a simple matter to obtain the corresponding asymptotic expression for  $\bar{\mathbf{F}}^{(2)}$  with the help of relation (13). The result is

$$\bar{\mathbf{F}}^{(2)} = \bar{\mathbf{F}} - \frac{c_0^{(1)}}{c_0^{(2)}} \mathbf{A}^{(1)} \delta \mathbf{Q} - \frac{c_0^{(1)}}{c_0^{(2)}} \mathbf{A}^{(2)} [\delta \mathbf{Q}, \delta \mathbf{Q}] + O(\delta \mathbf{Q}^3). \quad (36)$$

For later use, it is helpful to spell out the asymptotic expansions for the stored-energy functions  $W^{(1)}(\bar{\mathbf{F}}^{(1)})$  and  $W^{(2)}(\bar{\mathbf{F}}^{(2)})$ , which are needed in the computation of estimate (9). Thus, by making use of relation (35), we have that in the limit as  $\delta \mathbf{Q} \rightarrow \mathbf{0}$ :

$$W^{(1)}(\bar{\mathbf{F}}^{(1)}) = W^{(1)}(\bar{\mathbf{F}}) + \mathcal{S}^{(1)}(\bar{\mathbf{F}}) \cdot \mathbf{A}^{(1)} \delta \mathbf{Q} + \mathcal{L}^{(1)}(\bar{\mathbf{F}}) \cdot \mathbf{A}^{(2)} [\delta \mathbf{Q}, \delta \mathbf{Q}] + \frac{1}{2} \mathbf{A}^{(1)} \delta \mathbf{Q} \cdot \mathcal{L}^{(1)}(\bar{\mathbf{F}}) \mathbf{A}^{(1)} \delta \mathbf{Q} + O(\delta \mathbf{Q}^3). \quad (37)$$

Further, by making use of Eq. (36) together with relation (14) we have that

$$\begin{aligned} W^{(2)}(\bar{\mathbf{F}}^{(2)}) = & W^{(1)}(\bar{\mathbf{F}}) - \frac{c_0^{(1)}}{c_0^{(2)}} \mathcal{S}^{(1)}(\bar{\mathbf{F}}) \cdot \mathbf{A}^{(1)} \delta \mathbf{Q} + \mathcal{S}^{(1)}(\bar{\mathbf{F}}) \cdot \bar{\mathbf{F}} \delta \mathbf{Q} + \frac{c_0^{(1)}}{c_0^{(2)}} \mathcal{S}^{(1)}(\bar{\mathbf{F}}) \cdot \mathbf{A}^{(2)} [\delta \mathbf{Q}, \delta \mathbf{Q}] + \frac{(c_0^{(1)})^2}{2(c_0^{(2)})^2} \mathbf{A}^{(1)} \delta \mathbf{Q} \cdot \mathcal{L}^{(1)}(\bar{\mathbf{F}}) \mathbf{A}^{(1)} \delta \mathbf{Q} \\ & - \frac{c_0^{(1)}}{c_0^{(2)}} \mathcal{S}^{(1)}(\bar{\mathbf{F}}) \cdot \mathbf{A}^{(1)} \delta \mathbf{Q} \delta \mathbf{Q} - \frac{c_0^{(1)}}{c_0^{(2)}} \mathcal{L}^{(1)}(\bar{\mathbf{F}}) \mathbf{A}^{(1)} \delta \mathbf{Q} \cdot \bar{\mathbf{F}} \delta \mathbf{Q} + \frac{1}{2} \bar{\mathbf{F}} \delta \mathbf{Q} \cdot \mathcal{L}^{(1)}(\bar{\mathbf{F}}) \bar{\mathbf{F}} \delta \mathbf{Q} + O(\delta \mathbf{Q}^3). \end{aligned} \quad (38)$$

In addition, it proves useful to write down the asymptotic expansions for the corresponding stresses  $\mathcal{S}^{(1)}(\bar{\mathbf{F}}^{(1)})$  and  $\mathcal{S}^{(2)}(\bar{\mathbf{F}}^{(2)})$ , which are also needed in the computation of Eq. (9). The results read as follows:

$$\mathcal{S}^{(1)}(\bar{\mathbf{F}}^{(1)}) = \mathcal{S}^{(1)}(\bar{\mathbf{F}}) + \mathcal{L}^{(1)}(\bar{\mathbf{F}}) \mathbf{A}^{(1)} \delta \mathbf{Q} + O(\delta \mathbf{Q}^2) \quad (39)$$

and

$$\mathcal{S}^{(2)}(\bar{\mathbf{F}}^{(2)}) = \mathcal{S}^{(1)}(\bar{\mathbf{F}}) + \mathcal{S}^{(1)}(\bar{\mathbf{F}}) \delta \mathbf{Q}^T - \frac{c_0^{(1)}}{c_0^{(2)}} \mathcal{L}^{(1)}(\bar{\mathbf{F}}) \mathbf{A}^{(1)} \delta \mathbf{Q} + \mathcal{L}^{(1)}(\bar{\mathbf{F}}) \bar{\mathbf{F}} \delta \mathbf{Q} + O(\delta \mathbf{Q}^2). \quad (40)$$

At this stage, with the aid of expressions (35)–(40), it is straightforward to compute the asymptotic expansion for the effective stored-energy function (9) in the limit as  $\delta \mathbf{Q} \rightarrow \mathbf{0}$ . The result reads as follows:

$$\hat{W}(\bar{\mathbf{F}}) = W^{(1)}(\bar{\mathbf{F}}) + c_0^{(2)} \mathcal{S}^{(1)}(\bar{\mathbf{F}}) \cdot (\bar{\mathbf{F}} \delta \mathbf{Q}) + \frac{c_0^{(2)}}{2} \bar{\mathbf{F}} \delta \mathbf{Q} \cdot \mathcal{L}^{(1)}(\bar{\mathbf{F}}) \bar{\mathbf{F}} \delta \mathbf{Q} - \frac{c_0^{(1)}}{2} [\mathcal{S}^{(1)}(\bar{\mathbf{F}}) \delta \mathbf{Q}^T + \mathcal{L}^{(1)}(\bar{\mathbf{F}}) \bar{\mathbf{F}} \delta \mathbf{Q}] \cdot \mathbf{A}^{(1)} \delta \mathbf{Q} + O(\delta \mathbf{Q}^3). \quad (41)$$

Note that to *second order* in  $\delta \mathbf{Q}$  expression (41) depends on the linear correcting term  $\mathbf{A}^{(1)}$ , which is computed next.

In order to determine  $\mathbf{A}^{(1)}$ , we turn our attention to Eq. (12). In particular, we substitute relations (35) and (36) in Eq. (12) and subsequently expand in  $\delta \mathbf{Q}$  to generate a hierarchical system of equations for the unknown tensorial coefficients introduced in (35):  $\mathbf{A}^{(1)}$ ,  $\mathbf{A}^{(2)}$ , as well as for higher-order correcting terms. The first non-trivial equation, of order  $\delta \mathbf{Q}$ , can be shown to yield the following relation for  $\mathbf{A}^{(1)}$ :

$$\mathbf{A}^{(1)} \delta \mathbf{Q} = c_0^{(2)} \mathbf{P} [\mathcal{S}^{(1)}(\bar{\mathbf{F}}) \delta \mathbf{Q}^T + \mathcal{L}^{(1)}(\bar{\mathbf{F}}) \bar{\mathbf{F}} \delta \mathbf{Q}], \quad (42)$$

where the microstructural tensor  $\mathbf{P}$  is given by expression (44) in the main body of the text. The following hierarchical equations—which serve to determine  $\mathbf{A}^{(2)}$  and the higher-order correcting terms—will not be included here, since they are not relevant for our purposes.

Having determined relation (42), it is now a simple matter to establish that—to *second order* in  $\delta \mathbf{Q}$ —the tangent second-order estimate (9) for the effective stored-energy function of granular materials made up of two crystal orientations is given by

$$\begin{aligned} \hat{W}(\bar{\mathbf{F}}) = & W^{(1)}(\bar{\mathbf{F}}) + c_0^{(2)} \mathcal{S}^{(1)}(\bar{\mathbf{F}}) \cdot (\bar{\mathbf{F}} \delta \mathbf{Q}) + \frac{c_0^{(2)}}{2} \bar{\mathbf{F}} \delta \mathbf{Q} \cdot \mathcal{L}^{(1)}(\bar{\mathbf{F}}) \bar{\mathbf{F}} \delta \mathbf{Q} \\ & - \frac{c_0^{(1)} c_0^{(2)}}{2} [\mathcal{S}^{(1)}(\bar{\mathbf{F}}) \delta \mathbf{Q}^T + \mathcal{L}^{(1)}(\bar{\mathbf{F}}) \bar{\mathbf{F}} \delta \mathbf{Q}] \cdot \mathbf{P} [\mathcal{S}^{(1)}(\bar{\mathbf{F}}) \delta \mathbf{Q}^T + \mathcal{L}^{(1)}(\bar{\mathbf{F}}) \bar{\mathbf{F}} \delta \mathbf{Q}] + O(\delta \mathbf{Q}^3), \end{aligned} \quad (43)$$

where the microstructural tensor  $\mathbf{P}$  is given (in component form) by

$$P_{ijkl} = \frac{1}{4\pi \det \mathbf{Z}_0} \int_{\|\xi\|=1} \frac{(\mathcal{L}_{ipkq}^{(1)}(\bar{\mathbf{F}}) \xi_p \xi_q)^{-1} \xi_j \xi_l}{\|\mathbf{Z}_0^{-1} \xi\|^3} dS. \quad (44)$$

Note from Eq. (43) that to order 1 the effective behavior of the composite reduces to that of the homogeneous SC, as expected. Moreover, to order  $\delta \mathbf{Q}$ , the effective stored-energy function (43) coincides identically with the Voigt bound (Ogden, 1978):  $\hat{W}_{\text{Voigt}}(\bar{\mathbf{F}}) = c_0^{(1)} W^{(1)}(\bar{\mathbf{F}}) + c_0^{(2)} W^{(2)}(\bar{\mathbf{F}}) = c_0^{(1)} W^{(1)}(\bar{\mathbf{F}}) + c_0^{(2)} W^{(1)}(\bar{\mathbf{F}} + \bar{\mathbf{F}} \delta \mathbf{Q}) = c_0^{(1)} W^{(1)}(\bar{\mathbf{F}}) + c_0^{(2)} (W^{(1)}(\bar{\mathbf{F}}) + \mathcal{S}^{(1)}(\bar{\mathbf{F}}) \cdot (\bar{\mathbf{F}} \delta \mathbf{Q}) + O(\delta \mathbf{Q}^2))$ , also as expected. In this regard, it is important to recall that the Voigt bound depends only on the initial volume fraction of the phases (or one-point statistics),  $c_0^{(1)}$  and  $c_0^{(2)}$ , and contains no dependence on higher-order statistical information about the initial microstructure. On the other hand, to order  $\delta \mathbf{Q}^2$ , the exact asymptotic expression (43) is seen to depend on the microstructural tensor (44), which accounts for two-point statistics.

For completeness, it is also noted that in the limit as  $\delta\mathbf{Q} \rightarrow \mathbf{0}$  the average deformation gradients in the phases of the granular composite simplify to

$$\bar{\mathbf{F}}^{(1)} = \bar{\mathbf{F}} + c_0^{(2)} \mathbf{P}[\mathcal{L}^{(1)}(\bar{\mathbf{F}})\delta\mathbf{Q}^T + \mathcal{L}^{(1)}(\bar{\mathbf{F}})\bar{\mathbf{F}}\delta\mathbf{Q}] + O(\delta\mathbf{Q}^2), \quad (45)$$

$$\bar{\mathbf{F}}^{(2)} = \bar{\mathbf{F}} - c_0^{(1)} \mathbf{P}[\mathcal{L}^{(1)}(\bar{\mathbf{F}})\delta\mathbf{Q}^T + \mathcal{L}^{(1)}(\bar{\mathbf{F}})\bar{\mathbf{F}}\delta\mathbf{Q}] + O(\delta\mathbf{Q}^2), \quad (46)$$

which are exact to order  $\delta\mathbf{Q}$ .

## References

- Abeyaratne, R., Triantafyllidis, N., 1981. The emergence of shear bands in plane strain. *Int. J. Solids Struct.* 17, 1113–1134.
- Albalak, R.J., Thomas, E.L., 1993. Microphase separation of block copolymer solution in a flow field. *J. Polym. Sci. Part B: Polym. Phys.* 31, 37–46.
- Allan, P., Arridge, R.G.C., Ehtaiatkar, F., Folkes, M.J., 1991. The mechanical properties of an oriented lamella stock formed from an S–B–S block copolymer. *J. Phys. D* 24, 1381–1390.
- Arruda, E.M., Boyce, M.C., 1993. A three-dimensional constitutive model for the large stretch behavior of rubber elastic materials. *J. Mech. Phys. Solids* 41, 389–412.
- Bockstaller, M.R., Mickiewicz, R.A., Thomas, E.L., 2005. Block copolymer nanocomposites: perspectives for tailored functional materials. *Adv. Mater.* 17, 1331–1349.
- Brun, M., Lopez-Pamies, O., Ponte Castañeda, P., 2007. Homogenization estimates for fiber-reinforced elastomers with periodic microstructures. *Int. J. Solids Struct.* 44, 5953–5979.
- Cohen, Y., Albalak, R.J., Dair, B.J., Capel, M.S., Thomas, E.L., 2000. Deformation of oriented lamellar block copolymer films. *Macromolecules* 33, 6502–6516.
- Dair, B.J., Honeker, C.C., Alward, D.B., Avgeropoulos, A., Hadjichristidis, N., Fetters, L.J., Capel, M., Thomas, E.L., 1999. Mechanical properties and deformation behavior of the double gyroid phase in unoriented thermoplastic elastomers. *Macromolecules* 32, 8145–8152.
- Fredrickson, G.H., Bates, F.S., 1996. Dynamics of block copolymers: theory and experiment. *Annu. Rev. Mater. Sci.* 26, 501–550.
- Garcia, R., 2006. Etude du comportement sous déformation de copolymère à blocs SBS et SBM à morphologie lamellaire. Ph.D. Dissertation, L'Institut National des Sciences Appliquées de Lyon, France.
- Gent, A., 1996. A new constitutive relation for rubber. *Rubber Chem. Technol.* 69, 59–61.
- Geymonat, G., Müller, S., Triantafyllidis, N., 1993. Homogenization of nonlinearly elastic materials, microscopic bifurcation and macroscopic loss of rank-one convexity. *Arch. Ration. Mech. Anal.* 122, 231–290.
- Gido, S.P., Gunther, J., Thomas, E.L., 1993. Lamellar diblock copolymer grain boundary morphology. 1. Twist boundary characterization. *Macromolecules* 26, 4506–4520.
- Hill, R., 1972. On constitutive macro-variables for heterogeneous solids at finite strain. *Proc. R. Soc. London A* 326, 131–147.
- Honeker, C.C., Thomas, E.L., 1996. Impact of morphological orientation in determining mechanical properties in triblock copolymers. *Chem. Mater.* 8, 1702–1714.
- Honeker, C.C., Thomas, E.L., Albalak, R.J., Hadjuk, D.A., Gruner, S.M., Capel, M.C., 2000. Perpendicular deformation of a near-single crystal triblock copolymer with a cylindrical morphology. 1. Synchrotron SAXS. *Macromolecules* 33, 9395–9406.
- Knowles, J.K., Sternberg, E., 1975. On the ellipticity of the equations of nonlinear elastostatics for a special material. *J. Elasticity* 5, 341–361.
- Lopez-Pamies, O., 2008. A new hyperelastic model for rubber elastic materials, submitted for publication.
- Lopez-Pamies, O., Ponte Castañeda, P., 2006a. On the overall behavior, microstructure evolution, and macroscopic stability in reinforced rubbers at large deformations. I—Theory. *J. Mech. Phys. Solids* 54, 807–830.
- Lopez-Pamies, O., Ponte Castañeda, P., 2006b. On the overall behavior, microstructure evolution, and macroscopic stability in reinforced rubbers at large deformations. II—Application to cylindrical fibers. *J. Mech. Phys. Solids* 54, 831–863.
- Lopez-Pamies, O., Ponte Castañeda, P., 2008. Microstructure evolution in hyperelastic laminates and implications for overall behavior and macroscopic stability. *Mech. Mater.*, accepted for publication.
- Ogden, R., 1978. Extremum principles in non-linear elasticity and their application to composites—I. Theory. *Int. J. Solids Struct.* 14, 265–282.
- Park, C., Yoon, J., Thomas, E.L., 2003. Enabling nanotechnology with self assembled block copolymer patterns. *Polymer* 44, 6725–6760.
- Polis, D.L., Winey, K.I., 1998. Controlling kink band morphology in block copolymers: threshold criteria and stability. *Macromolecules* 31, 3617–3625.
- Ponte Castañeda, P., 1996. Exact second-order estimates for the effective mechanical properties of nonlinear composite materials. *J. Mech. Phys. Solids* 44, 827–862.
- Ponte Castañeda, P., 2002. Second-order homogenization estimates for nonlinear composites incorporating field fluctuations. I. Theory. *J. Mech. Phys. Solids* 50, 737–757.
- Ponte Castañeda, P., Suquet, P., 1998. Nonlinear composites. *Adv. Appl. Mech.* 34, 171–302.
- Ponte Castañeda, P., Tiberio, E., 2000. A second-order homogenization method in finite elasticity and applications to black-filled elastomers. *J. Mech. Phys. Solids* 48, 1389–1411.
- Ponte Castañeda, P., Willis, J.R., 1999. Variational second-order estimates for nonlinear composites. *Proc. R. Soc. London A* 455, 1799–1811.
- Prasman, E., Thomas, E.L., 1998. High-strain tensile deformation of a sphere-forming triblock copolymer/mineral oil. *J. Polym. Sci. Part B: Polym. Phys.* 36, 1625–1636.
- Read, D.J., Duckett, R.A., Sweeney, J., McLeish, T.C.B., 1999. The chevron folding instability in thermoplastic elastomers and other layered materials. *J. Phys. D* 32, 2087–2099.
- Seguela, R., Prud'homme, J., 1981. Deformation mechanism of thermoplastic 2-phase elastomer of lamellar morphology having a high volume fraction of the rubbery microphase. *Macromolecules* 14, 197–202.
- Triantafyllidis, N., Maker, B.N., 1985. On the comparison between microscopic and macroscopic instability mechanisms in a class of fiber-reinforced composites. *J. Appl. Mech.* 52, 794–800.
- Triantafyllidis, N., Nestorvić, N., 2005. Onset of failure in finitely strained layered composites subjected to combined normal and shear strain. *J. Mech. Phys. Solids* 52, 941–974.
- Triantafyllidis, N., Nestorvić, M.D., Schraad, M.W., 2006. Failure surfaces for finitely strained two-phase periodic solids under general in-plane loading. *J. Appl. Mech.* 73, 505–515.
- Tzianetopoulou, T., Boyce, M.C., 2004. Micromechanics of PS/PB/PS triblock-copolymer films with lamellar morphology. In: *Materials Research Society Symposium Proceedings*, vol. 788, p. L9.3.
- Willis, J.R., 1977. Bounds and self-consistent estimates for the overall moduli of anisotropic composites. *J. Mech. Phys. Solids* 25, 185–202.
- Willis, J.R., 1982. Elasticity theory of composites. *Mech. Solids* 653–686.